Buoyancy Forcing Dominates the Cross-Equatorial Ocean Heat Transport Response to Northern Hemisphere Extratropical Cooling

MATTHEW T. LUONGO,[a] SHANG-PING XIE,[a] AND IAN EISENMAN[a]

[a] *Scripps Institution of Oceanography, University of California, San Diego, La Jolla, California*

(Manuscript received 8 December 2021, in final form 20 June 2022)

ABSTRACT: Cross-equatorial ocean heat transport (OHT) changes have been found to damp meridional shifts of the intertropical convergence zone (ITCZ) induced by hemispheric asymmetries in radiative forcing. Zonal-mean energy transport theories and idealized model simulations have suggested that these OHT changes occur primarily due to wind-driven changes in the Indo-Pacific's shallow subtropical cells (STCs) and buoyancy-driven changes in the deep Atlantic meridional overturning circulation (AMOC). In this study we explore the partitioning between buoyancy and momentum forcing in the ocean's response. We adjust the top-of-atmosphere solar forcing to cool the Northern Hemisphere (NH) extratropics in a novel set of comprehensive climate model simulations designed to isolate buoyancy-forced and momentum-forced changes. In this case of NH high-latitude forcing, we confirm that buoyancy-driven changes in the AMOC dominate in the Atlantic. However, in contrast with prior expectations, buoyancy-driven changes in the STCs are the primary driver of the heat transport changes in the Indo-Pacific. We find that buoyancy-forced Indo-Pacific STC changes transport nearly 4 times the amount of heat across the equator as the shallower wind-driven STC changes. This buoyancy-forced STC response arises from extratropical density perturbations that are amplified by the low cloud feedback and communicated to the tropics by the ventilated thermocline. While the ocean's specific response is dependent on the forcing scheme, our results suggest that partitioning the ocean's total response to energy perturbations into buoyancy and momentum forcing provides basin-specific insight into key aspects of how the ocean damps ITCZ migrations that previous zonal-mean frameworks omit.

KEYWORDS: Atmosphere-ocean interaction; Energy transport; Meridional overturning circulation; Intertropical convergence zone

1. Introduction

One of the most coherent features of Earth as seen from space is a zonal band of clouds near the equator. This cloud band, referred to as the intertropical convergence zone (ITCZ; Waliser and Gautier 1993), is at the approximate location of time-mean maximum precipitation (e.g., Philander et al. 1996), as easterly surface trade winds converge over warm tropical waters, rise, cool, and precipitate out moisture (e.g., Mitchell and Wallace 1992). The zonal-mean position of the ITCZ is highly sensitive to differential hemispheric heating (e.g., Lindzen and Hou 1988; Mitchell and Wallace 1992; Chiang et al. 2003), spending Northern Hemisphere (NH) summer north of the equator and NH winter south of the equator.

In the annual mean, the equator receives more solar insolation than high latitudes. The atmosphere and ocean meridionally transport some of this excess energy and smooth the latitudinal energy gradient (e.g., Held 2001; Ganachaud and Wunsch 2003; Wunsch 2005; Czaja and Marshall 2006). By altering the planet's temperature gradient, this meridional energy transport is crucial in setting the location of Earth's energy flux equator, which roughly corresponds to the ITCZ's zonal-mean position (Broccoli et al. 2006; Kang et al. 2008; Schneider et al. 2014).

Naively, one might expect that because Earth's annual-mean insolation maximum is on the equator, seasonal migrations would average out and the ITCZ's annual-mean position would be situated squarely on the equator. In reality, however, the annual-mean ITCZ is north of the equator. A number of studies have explored the ITCZ's asymmetric climatology, suggesting both local drivers, such as coastal geometry (Xie and Philander 1994; Philander et al. 1996), and remote extratropical drivers (Chiang et al. 2003; Chiang and Bitz 2005; Broccoli et al. 2006; Kang et al. 2008).

The zonal-mean position of the ITCZ coincides with the rising branch of the Hadley cells (Xie 2004). In the tropical atmosphere, the thermally direct Hadley cells transport heat in the direction of their upper branch, leading to the so-called atmospheric energetic framework (Schneider et al. 2014; Kang et al. 2018; Hwang et al. 2021). In this framework, the atmosphere can balance the hemispheric heating asymmetry if the ITCZ shifts toward the warmer hemisphere. This basic diagnostic has been confirmed in modeling studies where the atmosphere is coupled to a motionless slab ocean and a hemispherically asymmetric heating is imposed at the ocean surface (Chiang and Bitz 2005; Broccoli et al. 2006; Kang et al. 2008, 2009).

However, the meridional circulation of the ocean is also a crucial player in setting the ITCZ position. In fact, using observational evidence and modeling, Frierson et al. (2013) and Marshall et al. (2014) point to ocean circulation as the driver of the NH-displaced ITCZ. In particular, both studies suggest that the Atlantic meridional overturning circulation (AMOC), which transports heat cross-equatorially from the Southern Hemisphere (SH) into the North Atlantic, warms

Supplemental information related to this paper is available at the Journals Online website: https://doi.org/10.1175/JCLI-D-21-0950.s1.

Corresponding author: M. T. Luongo, mluongo@ucsd.edu

DOI: 10.1175/JCLI-D-21-0950.1

the NH and creates the northward annual-mean displacement of the ITCZ.

The ITCZ's equilibrium position is clearly established as arising due to coupled ocean–atmosphere processes. However, because it takes many centuries for ocean processes to equilibrate to abrupt forcing (e.g., Held et al. 2010), the transient response of the ITCZ to interhemispheric forcing perturbations is what ultimately matters on societal time scales. This transient adjustment is less well understood.

Comprehensive global climate model (GCM) simulations that include a dynamic ocean exhibit less of an ITCZ shift than slab ocean model simulations relative to the same extratropical forcing perturbation from cloud brightness (Kay et al. 2016), ocean albedo (Hawcroft et al. 2017), sea ice (Tomas et al. 2016), aerosols (Hawcroft et al. 2018), or top-of-atmosphere (TOA) albedo forcing (Green and Marshall 2017; Yu and Pritchard 2019; Liu et al. 2021). In such coupled GCM simulations, the total ocean–atmosphere system responds to the same interhemispheric radiative imbalance that solely the atmosphere responds to in slab ocean simulations (Chiang and Bitz 2005; Broccoli et al. 2006; Kang et al. 2008, 2009). The ocean heat transport leads to a reduction in the magnitude of the atmospheric energetic transport response. However, the specific mechanisms by which ocean dynamics buffer ITCZ shifts remains an open question.

Two main mechanisms have been proposed to explain the ocean's ability to damp ITCZ shifts and help to understand the transient climate response. The first mechanism is buoyancy-focused and suggests that the AMOC, in addition to setting the ITCZ's mean state, responds to density-driven buoyancy anomalies by transporting anomalous energy across the equator. In doing so, the AMOC reduces both the hemispheric heating asymmetry and resulting ITCZ migration (Frierson et al. 2013; Fučkar et al. 2013; Marshall et al. 2014; He et al. 2019; Yu and Pritchard 2019). Recently, Yu and Pritchard (2019, hereafter YP19) explored the AMOC's response to imposed interhemispheric TOA solar insolation perturbations at different latitudes in a comprehensive GCM. YP19 found that AMOC responses are of primary importance in muting asymmetric energetic forcing, monotonically increasing with forcing latitude such that the entire ocean–atmosphere energy transport system becomes more ocean-dominated as the TOA forcing perturbation reaches higher latitudes.

The other ocean response often proposed as a damping mechanism for ITCZ shifts is momentum-focused. This pathway emphasizes the mechanical coupling between the easterly trade winds in the lower Hadley cell and the subtropical cells (STCs) in the ocean via Ekman transport (Held 2001; Schneider et al. 2014; Kay et al. 2016; Schneider 2017; Green and Marshall 2017; Kang et al. 2018; Green et al. 2019). In this framework, as the ITCZ shifts toward the warmer hemisphere in response to a forcing perturbation, so too do the STCs. Shifted toward the warmer hemisphere, the upper branches of the STCs transport heat cross-equatorially into the cooler hemisphere and mute ITCZ shifts. In a highly idealized study, Green and Marshall (2017, hereafter GM17) explore this pathway by cooling the NH and heating the SH. GM17 find that the modeled ocean circulation changes strongly damp ITCZ shifts compared to a model with a motionless slab ocean. They identify anomalous easterly trade winds, which drive anomalous cross-equatorial Ekman flow in the upper tropical ocean, as a potential cause of this ocean damping. In a follow-up study, Green et al. (2019) impose energetic perturbations at numerous latitudes and find that the modeled ocean circulation always damps ITCZ shifts relative to a slab ocean configuration and that this damping is strongest when the forcing is polar amplified.

Although these studies provide a clear starting point toward understanding how the cross-equatorial ocean response to interhemispheric energy forcing mutes ITCZ shifts, a better understanding of the physical mechanisms at work is called for. In particular, the partitioning between buoyancy and momentum forcing in the ocean's circulation response has been largely ignored. To explore this problem, we present results from three sets of comprehensive GCM simulations that were designed to systematically isolate the drivers of the ocean's transient response to hemispheric forcing. We employ an idealized, zonally uniform TOA solar insolation reduction from 45° to 65°N following the NH extratropical experiment of the Extratropical–Tropical Interaction Model Intercomparison Project (Kang et al. 2019) in order to induce a southward ITCZ shift and a northward ocean heat transport response. We adopt a method of wind stress overriding (Gregory et al. 2016; Liu et al. 2018; Larson et al. 2018, 2020; Liu et al. 2021) to mechanically decouple the surface ocean from the atmosphere. Through this partial decoupling we can cleanly parse different ocean heat transport responses as solely buoyancy driven or solely momentum-driven.

Our results suggest that buoyancy forcing largely drives ocean heat transport changes in response to NH extratropical TOA insolation reduction. This includes the Atlantic's cross-equatorial heat transport, dominated by thermohaline-driven changes in the AMOC, but also the cross-equatorial heat transport in the Indo-Pacific STCs. In contrast with previous studies that assumed heat transport changes in the STCs were primarily momentum driven (e.g., GM17), we find that the dominant change is due to thermohaline-forced surface density perturbations inducing an anomalous shallow meridional overturning circulation (MOC) within the STCs. The buoyancy-forced response of the STCs, deeper and more asymmetric than the momentum-forced response, allows for efficient cross-equatorial heat transport. The detailed structure of this buoyancy-forced MOC has important implications for how the ocean translates thermohaline anomalies into anomalous advection.

The remainder of this paper is laid out as follows. Section 2 describes the experimental setup of our GCM simulations. Sections 3 and 4 present our primary results, with the former focused on the global and Atlantic zonal-mean response and the latter focused on the Indo-Pacific response. Section 5 discusses the anomalous, buoyancy-forced MOC in the Indo-Pacific and its implications, as well as limitations of the current work and potential next steps. Finally, section 6 summarizes and concludes.

2. GCM simulations

We use version 1.2.2 of the Community Earth System Model (CESM; Hurrell et al. 2013) from the National Center for Atmospheric Research (NCAR). CESM is configured with active atmosphere (CAM5; Neale et al. 2010), ocean (POP2; Smith et al. 2010), land surface (CLM4; Lawrence et al. 2012), and sea ice (CICE4; Holland et al. 2012) components interactively connected via the model's coupler (CPL7; Craig 2014). The components are run in the standard, coupled preindustrial mode (the "B_1850_CAM5" component set) with the atmosphere and land components run on a nominal 2° horizontal grid and the ocean and sea ice components run on a nominal 1° horizontal grid ("f19gx1v6" horizontal resolution). The atmosphere and ocean components have 26 and 60 vertical layers, respectively.

The atmosphere is thermodynamically coupled to the ocean via the total surface heat flux, Q_{net} (e.g., Xie et al. 2010; Liu et al. 2018; Hu et al. 2020), and variations in Q_{net} patterns affect circulation in the atmosphere and ocean. Anthropogenic aerosols, an important driver of historical patterns of climate change (e.g., Deser et al. 2020; Kang et al. 2021), have historically been primarily emitted from NH industrial centers (Wang et al. 2015). Thus, due to short atmospheric residence times, aerosols have induced a hemispherically asymmetric Q_{net} forcing response qualitatively similar to prior studies that applied anomalous heating to motionless slab ocean models to induce ITCZ shifts in atmosphere-only GCMs (e.g., Chiang et al. 2003; Chiang and Bitz 2005; Broccoli et al. 2006; Kang et al. 2008, 2009).

With this in mind, we force CESM with an asymmetric radiative forcing analogous to aerosol forcing to elicit a clear meridional ITCZ shift. We follow the experimental protocol of the NH extratropical experiment of the Extratropical–Tropical Interaction Model Intercomparison Project (ETINMIP: Kang et al. 2019), which has an abrupt reduction in TOA solar flux within 45°–65°N (Fig. S1 in the online supplemental material). Although this forcing is time-varying as a result of seasonal and diurnal insolation cycles, ETINMIP forcing corresponds to an annual-mean, zonal-mean maximum forcing of about 45 W m^{-2} at 55°N. Though the forcing is applied in the NH extratropics, the globally averaged, annual-mean forcing of approximately -1.6 W m^{-2} is similar to the historical annual-mean aerosol forcing estimate given in the IPCC Sixth Assessment Report (Forster et al. 2021). The reduction in NH TOA insolation in our simulations is expected to cool the surface. We expect the climate to respond to this imposed interhemispheric heating asymmetry and smooth the hemispheric energy gradient by increasing both northward atmospheric heat transport, corresponding to a southward shift of the ITCZ, and northward ocean heat transport (OHT).

To test the assumption that the transient OHT response of the AMOC would be primarily buoyancy-forced and the transient OHT response of the STCs would be primarily momentum-forced, we adopt the approximation that the total transient response of the ocean to the change in TOA insolation is the linear sum of the ocean's response to the change in surface buoyancy flux and the ocean's response to the change in surface wind stress. This is schematically illustrated in Fig. 1. A change in TOA insolation S_0 is communicated through the atmosphere to the ocean surface. This leads to a response in the ocean state T, due to changes in the surface buoyancy flux B, which includes net shortwave and net longwave radiative fluxes, sensible and latent turbulent energy fluxes, and net precipitation. Additionally, S_0 affects the atmospheric circulation and hence the surface wind stress τ, which affects the ocean by causing changes in Ekman flow. Large red arrows in Fig. 1 represent these two pathways. It should be noted that we do not account for effects that would be seen as nonlinearities in this framework. Our results in sections 3 and 4 show that these nonlinearities are relatively small for the cross-equatorial ocean heat transport that we focus on in this study.

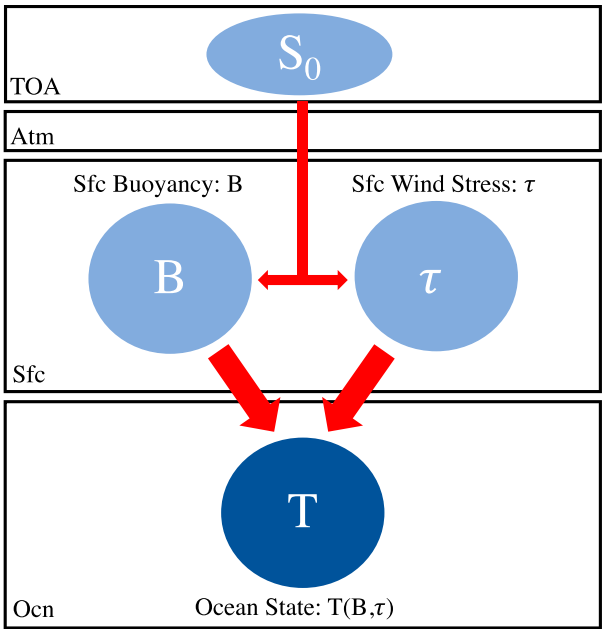

FIG. 1. Schematic of the framework adopted in this study. The change in TOA insolation (S_0) is communicated through the atmosphere to influence the ocean state (T) via changes in the surface buoyancy flux (B) and surface wind stress (τ). Here we separate these two changes in the ocean surface forcing. Large red arrows denote the effects of the surface fluxes on the ocean state. Smaller red arrows denote the effects of the insolation forcing on the ocean surface forcing. The four boxes correspond to domains in the climate system where these pathways are communicated: top-of-atmosphere (TOA), atmosphere (Atm), surface (Sfc), and ocean (Ocn).

Based on this decomposition, we perform wind stress overriding experiments where we mechanically decouple the model's ocean from the atmosphere by locking wind stress over the ocean via a novel method created for this study. In the standard CESM setup, CPL7 couples the ocean to the atmosphere once per day. We introduce a protocol to output the zonal and meridional wind stress (fields contained within the "x2o_oo" variable) at each of these coupling steps. We then save the wind stress and allow it to be specified in

TABLE 1. The five CESM cases that we run for each ensemble set, indicating the simulation length (duration), whether we output the surface wind stress (CPL output), whether we specify the surface wind stress from another run (τ-lock), and whether we reduce the insolation from 45° to 65°N (TOA reduction). The names of the last three simulations indicate whether the wind stress is specified from Clim1 (Tau1 …) or from Clim2 (Tau2 …) and whether the insolation is left at its default value (… S1) or reduced (… S2).

Case	Duration	CPL7 output	τ-lock	TOA reduction
Clim1	51 yr	✓	×	×
Clim2	50 yr	✓	×	✓
Tau1S1	50 yr	×	✓	×
Tau1S2	50 yr	×	✓	✓
Tau2S1	50 yr	×	✓	×

another simulation such that the ocean sees identical wind stress fields in both simulations.

We emphasize that this wind stress locking methodology allows us to exactly specify the ocean surface wind stress field from a separate simulation. After the first day of each simulation (since the first coupling step happens near the start of the second day), the ocean surface wind stress field is identical in the two simulations. This approach is inspired by Liu et al. (2018), who overrode wind stress in GCM simulations using an approximate locking approach. Several other studies have also mechanically decoupled the ocean from the atmosphere via wind stress overriding in CESM, but these studies have typically input climatological wind stress rather than the full time-evolving wind stress field (Gregory et al. 2016; Larson et al. 2018, 2020; Liu et al. 2021). By design, using the climatology leads to differences in the wind stress fields between the two simulations. The method we adopt eliminates this residual entirely and allows for precise comparison between two cases. In addition, by using the full time evolution of the wind stress field, we are able to maintain internal variability in the wind stress which can influence the state of the ocean.

We run five CESM cases designed to systematically isolate the fully coupled, buoyancy-forced, and momentum-forced ocean response to decreased NH TOA insolation (see Table 1). The first is a default preindustrial simulation with greenhouse gas concentrations and other forcings set to 1850 levels ("Clim1"), and the second is a standard ETINMIP NH extratropical experiment which is identical to Clim1 except that the TOA insolation is reduced from 45° to 65°N as described above ("Clim2"). We output the ocean surface wind stress at each coupling step for each of these simulations. The next simulation is forced identically as Clim1 except that the ocean is mechanically decoupled from the atmosphere via wind stress overriding ("Tau1S1"). Overriding wind stress and decoupling the ocean from the atmosphere inevitably influences the climate: the simulated fields in Tau1S1 are similar but not identical to Clim1 (see Figs. S2j–l, for example). However, overriding does not appear to introduce substantial climate drift (Fig. S3) and any residuals between the coupled and decoupled cases that are introduced by wind stress overriding are smaller than the forced response we focus on presently. Nevertheless, in order to compare only simulations that are decoupled, thus comparing like to like, we treat the Tau1S1 simulation as the "control" climate for comparison with other cases with wind stress overriding. To create Tau1S1 we offset the input wind stress by one year (i.e., we prescribe the year $n + 1$ ocean surface wind stress from Clim1 during year n of Tau1S1). The first "test" simulation has the NH TOA insolation reduced but has the ocean surface wind stress prescribed from Clim1 ("Tau1S2"), and the second "test" simulation has standard NH TOA insolation but has the ocean surface wind stress prescribed from Clim2 ("Tau2S1").

Using the output of these five simulations, we identify the fully coupled ("FC"), radiatively/buoyancy-forced ("BF"), and wind stress/momentum-forced ("MF") climate responses to the reduction in NH TOA insolation as follows:

$$\mathrm{FC} = \mathrm{Clim2} - \mathrm{Clim1}, \tag{1}$$

$$\mathrm{BF} = \mathrm{Tau1S2} - \mathrm{Tau1S1}, \tag{2}$$

$$\mathrm{MF} = \mathrm{Tau2S1} - \mathrm{Tau1S1}. \tag{3}$$

The FC response illustrates the freely evolving, total climate response to our NH extratropical TOA perturbation by comparing Clim2 with the fully coupled control, Clim1. The BF response captures the forced response that results from radiatively induced buoyancy anomalies by comparing Tau1S2, where radiative forcing is applied but unforced wind stress is specified, with the decoupled control run, Tau1S1. Finally, the MF response illustrates the forced response that results from wind stress–induced momentum anomalies alone by comparing Tau2S1, which has wind stress specified from Clim2 but does not have radiative perturbations, with Tau1S1.

In these equations, the linear approximation illustrated in Fig. 1 takes the form that the fully coupled response is approximately equal to the sum of the buoyancy-forced and momentum-forced responses:

$$\mathrm{FC} = \mathrm{BF} + \mathrm{MF} + \mathrm{Residual} \approx \mathrm{BF} + \mathrm{MF}, \tag{4}$$

where the Residual term includes momentum decoupling effects and nonlinear effects in the response of the ocean to changes in surface forcing.

Finally, to address the effects of simulated internal climate variability, we run three realizations of each of the five cases presented in Table 1 with different initial conditions, yielding 15 cases total. Following the CESM Large Ensemble protocol (Kay et al. 2015), differences in initial conditions are generated

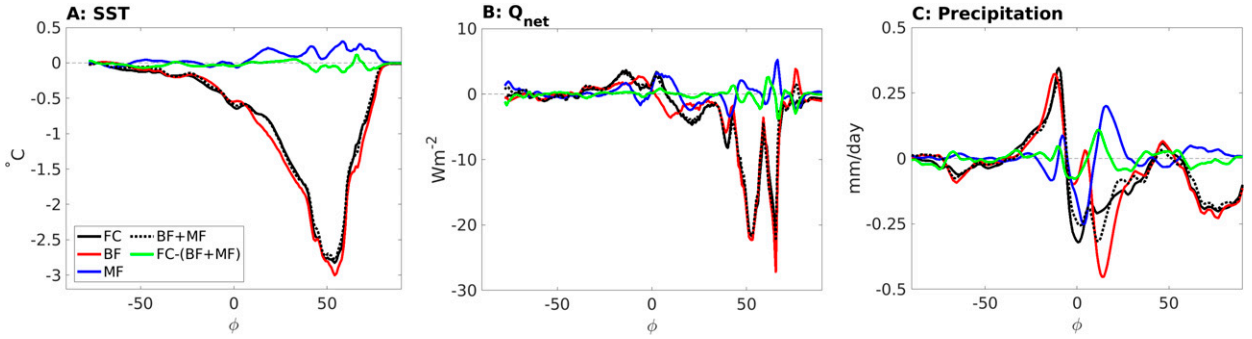

FIG. 2. (a) Zonal-mean SST anomalies in the FC (solid black), BF (red), MF (blue), BF + MF (dotted black), and FC − (BF + MF) (green) climate responses. A zero line is plotted as the thin, dashed black line. (b) Zonal-mean Q_{net} response with colors as in (a). (c) Zonal-mean precipitation response with colors as in (a). The color scheme is this figure is continued throughout the remainder of this article.

by introducing a round-off error sized perturbation [$O(10^{-14})$ K] to the atmospheric temperature field. For each of the five cases, we take the ensemble mean among the three realizations in order to minimize the effects of internal variability. While adding more ensemble members would further reduce the internal variability, the results suggest that three ensemble members are sufficient for the purposes of the present study. Last, to provide the ocean sufficient time to spin up in response to the abrupt TOA forcing and to average out internal climate variability further, we focus on the last 40 years of the 50-yr simulations. In the remainder of the paper, all results presented are ensemble means among the three realizations averaged over years 11–50, unless otherwise stated.

3. Global and Atlantic zonal-mean responses

a. *Forced response of zonal-mean global Q_{net}*

Figure 2 presents the zonal-mean SST, Q_{net}, and total precipitation anomalies in the FC (black), BF (red), MF (blue), and Residual (green) responses. In these plots, the dotted black line is the sum of the BF and MF responses; the agreement between the solid and dotted black lines serves as an approximate validation of our approach which treats the FC response as the sum of the BF and MF responses. Because the maximum reduction in TOA insolation occurs at 55°N, the largest zonal-mean SST cooling occurs near this latitude (Fig. 2a). Throughout this region, the FC and BF responses are approximately equivalent and are roughly an order of magnitude larger than either the MF or Residual responses. Most noticeably, the FC and BF responses plunge to nearly 3°C cooling near 55°N, whereas the MF and Residual responses remain within ±0.2°–0.3°C. Aside from being smaller in magnitude, the MF response is also positive, opposing the strong cooling of the FC and BF responses and actually warming the NH extratropics. Overall, the FC and BF responses agree quite well in terms of magnitude and sign across all latitudes. While it is somewhat expected that a negative radiative perturbation would drive a strong buoyancy-forced negative SST response, the agreement between the FC and BF response is striking. This suggests, perhaps unsurprisingly, that buoyancy forcing dominates the zonal-mean SST response to NH extratropical forcing in the coupled climate system.

In Fig. 2b, the FC and BF zonal-mean Q_{net} responses are also approximately equivalent in the NH extratropics; the FC response is almost visually indistinguishable from the BF response near 55°N. The dominance of buoyancy forcing in the freely evolving coupled climate response is less robust in the tropics, where the momentum-forced MF response also contributes substantially to changes in surface heat flux via Ekman transport. However, the FC, BF, and MF responses are all of similar magnitude in the tropics, and the Residual response is considerably smaller. Considered together, the close agreement between the solid and dotted black lines in Figs. 2a and 2b suggests that the freely evolving zonal-mean response of important thermodynamic variables for ocean–atmosphere interactions is primarily a linear combination of buoyancy and momentum forcing. Put another way, FC ≈ BF + MF, and the approximation of the ocean's physical response to transient forcing proposed in Fig. 1 holds.

b. *Resulting ITCZ shift*

A strong positive SH precipitation anomaly is present in both the FC and BF responses in Fig. 2c. If we assume that the ITCZ location roughly corresponds to the latitude of the time-mean maximum precipitation (Philander et al. 1996), this SH precipitation peak affirms our intuition that the negative NH Q_{net} response seen in Fig. 2b induced a southward ITCZ shift. This SH positive precipitation anomaly in FC and BF is accompanied by a negative anomaly slightly north of the equator, where the ITCZ resides in the control simulation. However, the location and partition of the negative anomalies in the NH varies between FC and BF. In fact, a simple visual comparison suggests that the MF response plays a larger role in setting the FC zonal-mean precipitation response than it does for either the zonal-mean SST or Q_{net} FC responses, both of which are nearly entirely explained by BF. In FC, the largest negative precipitation anomalies are nearly on the equator and fairly well explained by momentum forcing in MF. In BF, the largest negative anomalies are farther north

and strongly opposed by MF, leading to a damped FC response at that latitude. Nevertheless, we find that the solid and dotted black lines still agree reasonably well.

Coinciding with the rising branch of the Hadley circulation, this ITCZ shift is also prominent in the atmospheric mass meridional overturning circulation streamfunction Ψ_A (note that the subscript A is used to distinguish atmospheric variables from their oceanic counterparts in this variable and throughout the paper). Following Döös and Nilsson (2011), we calculate Ψ_A as

$$\Psi_A(\phi,p,t) = a\cos\phi \oint\int_0^p \frac{v_A(\lambda,\phi,p',t)}{g}\,dp'\,d\lambda. \qquad (5)$$

Above, ϕ is latitude, λ is longitude, a is the radius of Earth approximated as 6371 km, g is gravitational acceleration, and p is pressure as a vertical coordinate with p' serving as a dummy integration variable. The Ψ_A responses are presented in Figs. 3a–c, and Fig. 3d shows the value of Ψ_A at the 700-hPa atmospheric level.

In the FC response in Fig. 3a, there is hemispherically asymmetric anomalous clockwise motion in both the NH and SH. This increased clockwise motion corresponds to a spinup of the NH Hadley cell and an even stronger spindown of the SH Hadley cell. Considered in tandem, this NH spinup and SH spindown will lead to a southward shift of the ITCZ. The BF Ψ_A response also consists of anomalous clockwise rotation in the NH and SH; however, unlike in the FC response, the BF Hadley cell response is stronger in NH than in SH. The FC anomalous Hadley cell response is mirrored relatively well by combining BF and MF as seen in the comparison of the solid and dotted black lines of Fig. 3d. The BF response provides a background state of anomalous clockwise rotation in both hemispheres and, although substantially smaller in magnitude, the MF response provides anomalous counterclockwise rotation in NH to cancel out some of the excess clockwise rotation seen in the BF response.

Importantly, the anomalous Hadley cell widths are narrower than the climatological Hadley cell widths, extending at most to around 15°S–20°N, as opposed to 30°S–30°N in the climatological circulation. Anomalous Hadley cell responses that are narrower than the climatology are also seen in Wang et al. (2016), Amaya et al. (2018), and Kang et al. (2021). This narrow width is a potential constraint on the width of the mechanically coupled Indo-Pacific STC response. In particular, the stronger and wider BF Ψ_A response is indicative of a stronger and deeper STC response than the weaker and narrower MF Ψ_A response.

c. *OHT as the driver of global Q_{net} trends*

An interhemispheric difference in zonally integrated Q_{net} is associated with a change in the zonally integrated ocean heat storage (OHS) and/or zonally integrated ocean heat horizontal divergence (OHD), where both OHS and OHD refer to vertically integrated quantities. Because OHT is simply the meridional integral of zonally integrated OHD, a change in Q_{net} is associated with a change in OHT, which qualitatively explains why ocean dynamics damp ITCZ migrations. A full

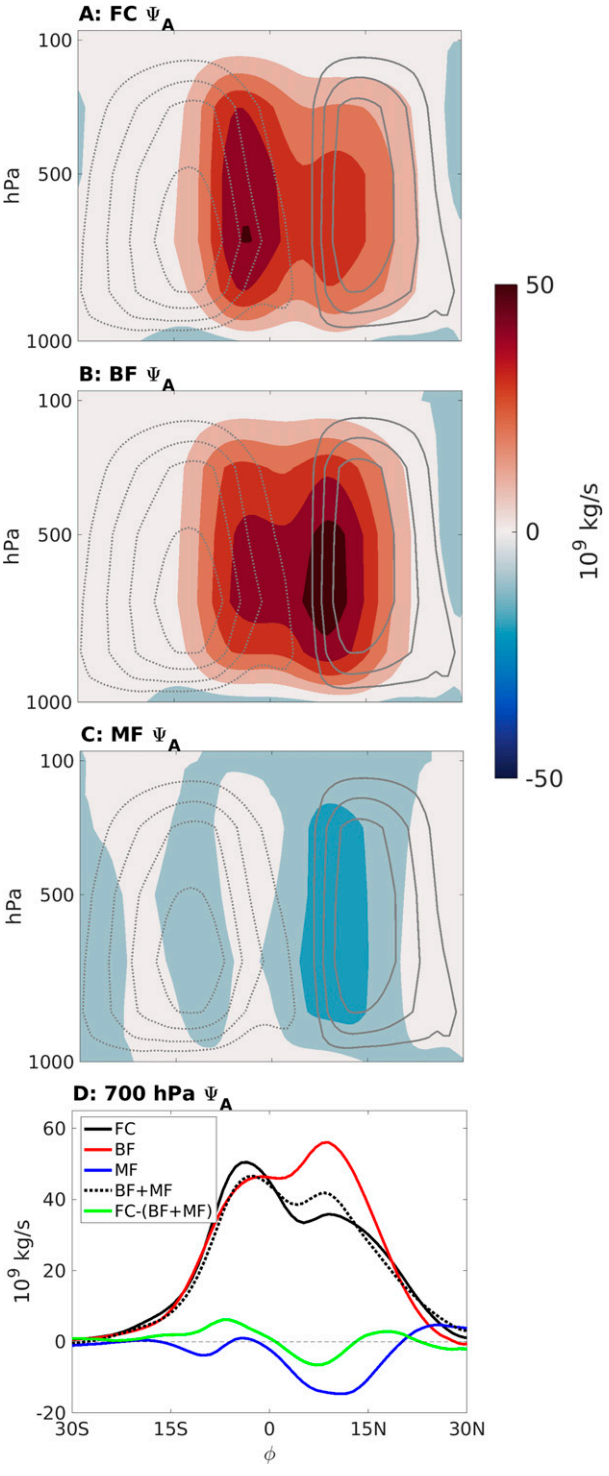

FIG. 3. (a) FC response (color fill) of the mass meridional overturning circulation Ψ_A with contours of 10^{10} kg s^{-1}. The time average of the unperturbed Ψ_A in the control climate, Clim1, is given as gray contours of 50^{10} kg s^{-1}, with solid positive (clockwise rotation) contours, dotted negative (counterclockwise rotation) contours, and the zero contour omitted. (b) BF response of Ψ_A, with color fill and contours as in (a). (c) MF response of Ψ_A, with color fill and contours as in (a). (d) 700-hPa value of Ψ_A, with colors as in Fig. 2.

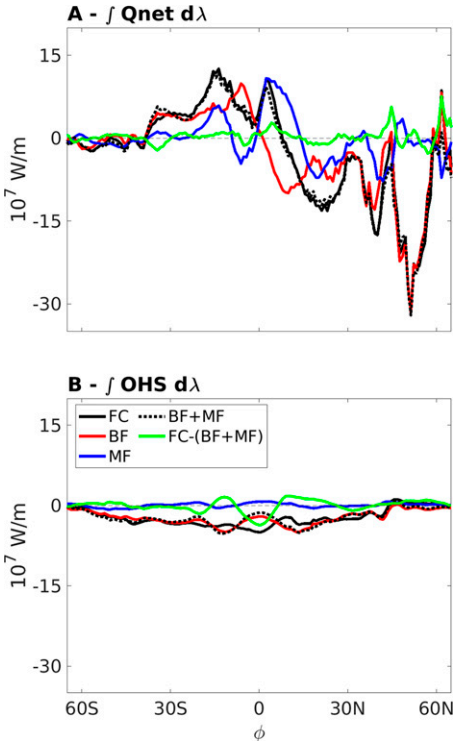

FIG. 4. (a) Zonally integrated net surface heat flux, Q_{net} [Eq. (A1)], with colors as in Fig. 2. (b) Zonally integrated ocean heat storage, OHS [Eq. (A3)], with colors as in Fig. 2.

derivation relating changes in Q_{net} to changes in OHS and OHD is available in the appendix. Due to the approximate linearity of global mean OHC trends (Fig. S4), we estimate OHS via the 40-yr linear trend of OHC and find that changes in zonally integrated OHS are substantially smaller than changes in zonally integrated Q_{net} (cf. Figs. 4a and 4b). Thus we neglect the influence of OHS on Q_{net} and make the approximation that

$$a\cos\phi\int_{\lambda_e}^{\lambda_w} Q_{\text{net}}\,d\lambda \approx a\cos\phi\int_{\lambda_e}^{\lambda_w} \text{OHD}\,d\lambda, \tag{6}$$

where λ_w is the western edge of a basin, λ_e is the eastern edge of a basin, and other variables are defined as above. With this approximation, we focus on OHD, and therefore OHT by Eq. (A6), as the driver of cross-equatorial Q_{net} asymmetries that can affect ITCZ migration. Put another way, we investigate ocean circulation as the primary driver of changes in Q_{net}, as opposed to local storage of heat in the water column.

CESM computes OHT for the global ocean (Fig. 5a) and the Atlantic basin (Fig. 5b) and the difference between the two corresponds to the Indo-Pacific basin's OHT (Fig. 5c). The global FC OHT response (black line in Fig. 5a) is positive throughout the tropics and subtropics and peaks at around 0.45 PW, about a quarter of the maximum total OHT in Clim1 (e.g., Fig. S5a), just north of the equator. The positive cross-equatorial FC OHT response, created by positive FC OHT contributions in both the Atlantic (Fig. 5b) and Indo-Pacific (Fig. 5c), damps imposed NH cooling by transporting heat northward across the equator.

Even with just three ensemble members, the ensemble-mean Residual OHT response in Fig. 5a is considerably smaller than the individual ensemble members' Residual OHT responses (cf. Fig. 5a with Figs. S6a,d,g). This suggests that much of the FC OHT response not explained by the BF or MF responses results from internal variability rather than from nonlinear responses or mechanical decoupling. The internally driven Residual OHT response in Fig. 5a is small compared to FC throughout the tropics and subtropics, further justifying the approximation of the ocean's full response to be a linear superposition of the ocean's responses to buoyancy and momentum forcing (Fig. 1).

However, BF and MF do not contribute with comparable magnitudes. Rather, the vast majority of the global FC response throughout the NH and SH tropics and midlatitudes seen in Fig. 5a results from buoyancy forcing changes captured by the BF response. In fact, the BF cross-equatorial OHT response is an order of magnitude larger than the MF response, which is closer in magnitude to the Residual response than to the BF response. This leads to the first important result of this study: buoyancy forcing is the primary driver of the global ocean response to radiative forcing from an NH extratropical TOA insolation reduction.

d. Buoyancy-driven Atlantic OHT and AMOC

The ocean's Eulerian-mean MOC (Ψ) as a function of latitude ϕ and depth z is calculated as

$$\Psi(\phi,z) = a\cos\phi\int_{z}^{0}\int_{\lambda_w}^{\lambda_e} v(\lambda,\phi,z')\,d\lambda\,dz', \tag{7}$$

where v is model-resolved meridional velocity in the ocean and z' is a dummy integration variable. CESM outputs a global and Atlantic Ψ (the AMOC) as history fields.

The AMOC is well known to be influenced by thermohaline processes (e.g., Kuhlbrodt et al. 2007; Buckley and Marshall 2016; Johnson et al. 2019; Yu and Pritchard 2019; Larson et al. 2020). The AMOC's surface branch transports warm, saline water from the subtropics into the North Atlantic. As these waters move farther north, they cool, become denser, and ultimately convect. After convecting, these deep waters move southward, closing the loop and connecting with the rest of the global overturning circulation in the Southern Ocean (Talley et al. 2011). Varying any of the thermohaline boundary conditions can cause changes in the AMOC strength, which has been suggested to have occurred at times in the paleoclimate record (e.g., Manabe and Stouffer 1997, 1999; Broecker 1997, 2003; Eisenman et al. 2009; Zhu et al. 2014).

Because the AMOC is the main driver of OHT in the Atlantic (Frierson et al. 2013; Marshall et al. 2014), we expect the buoyancy-forced BF response to dominate the multidecadal Atlantic OHT response, much as it dominates the global response as discussed in section 3c. A

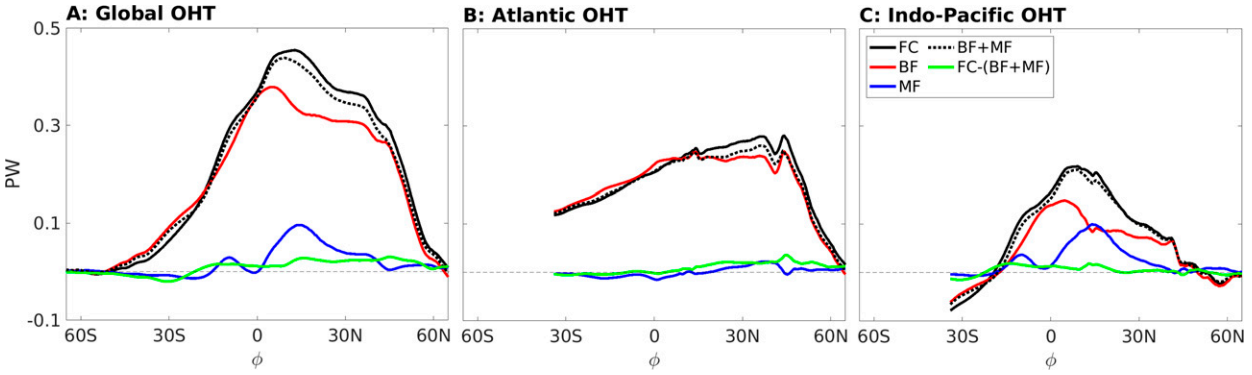

FIG. 5. (a) Global OHT response with colors as in Fig. 2. (b) Atlantic OHT response with colors as in Fig. 2. (c) Indo-Pacific OHT response with colors as in Fig. 2.

naive understanding of the BF-dominated global OHT response might therefore suggest that the AMOC dominates the total OHT response, while the OHT contribution from the STCs, which are often assumed to be momentum-forced, is negligible. However, we see in Figs. 5b and 5c that both the Atlantic and Indo-Pacific are in fact contributing to OHT, so we explicitly test these two transient response theories by considering the basin decomposition of OHT. As expected, the Atlantic's buoyancy-forced BF response encapsulates the vast majority of the FC response, with the momentum-forced MF response being nearly negligible even in the tropics. BF dominates tropical and cross-equatorial OHT to such an extent that the FC response can be approximated by the BF result alone.

The AMOC responses in Figs. 6d and 6e support the interpretation from Fig. 5b that the Atlantic OHT response is buoyancy dominated. Note that this applies only if the OHT changes are driven by circulation changes rather than temperature changes, which will be investigated below. With a Pearson product-moment coefficient of linear correlation (pattern correlation) of 0.995, the FC and BF AMOC patterns are nearly indistinguishable to the eye. On the other hand, the MF AMOC barely registers a circulation (Fig. 6f). Therefore, another important result from our wind stress overriding simulations is that the transient response of the AMOC to NH extratropical radiative forcing is nearly entirely buoyancy driven. This complements the results of Larson et al. (2020), who used a different wind stress overriding technique to find that buoyancy forcing sets the AMOC's equilibrium response.

It is worth pointing out that the AMOC response in our simulations is large. With a maximum value on the order of 10 Sv (1 Sv $\equiv 10^6$ m^3 s^{-1}), the FC and BF responses represent a considerable increase over the annual mean AMOC strength in the control climate (gray contours in Figs. 6d–f). Despite the slightly different forcing schemes between studies, the strong AMOC response in our simulations is qualitatively similar to the ΔHIGHLAT AMOC response of YP19. By varying the latitude of the TOA forcing, YP19 found that higher-latitude forcing monotonically led to a stronger AMOC response and more ocean-centric damping of ITCZ shifts. Considering this, our robust AMOC response from NH TOA forcing of 45°–65°N is unsurprising; we have effectively forced the climate system where it can elicit a strong AMOC response.

4. Indo-Pacific response

a. *Basinwide response*

Although previous understandings of meridional energy transport changes in response to changes in midlatitude heating have largely rested upon a zonal-mean description of Q_{net} anomalies, Fig. 7 illustrates rich zonal structures of SST, Q_{net}, and near-surface 850-hPa wind. Because the importance of buoyancy forcing in the fully coupled extratropical response is emphasized by the zonal-mean response of SST and Q_{net} in Figs. 2a and 2b, we pay particular attention to the FC and BF response of SST, Q_{net}, and near-surface wind in Figs. 7a and 7b.

The Pacific basin's NH extratropical SST and Q_{net} structure is distinctly rich. While negative SST anomalies are largest in the Bering Sea directly below the perturbation latitude, SST cooling is intensified over the eastern subtropical Pacific as well. A strengthened subtropical high over the north central Pacific in FC and BF leads to anomalous anticyclonic near-surface geostrophic winds. Cold advection from these anomalous northerly winds in the atmospheric boundary layer cools SST further and extends the temperature anomalies along the North American west coast into the eastern subtropical Pacific's low-cloud-dominated regime. This region also happens to be the "exchange window" for perturbations to reach the equatorial Pacific (Liu 1994; Nonaka et al. 2000). Although clearer in the BF response, the anomalous anticyclonic winds extend farther southwestward in both FC and BF from the eastern subtropical Pacific's SST cool tongue and drive a strongly negative Q_{net} anomaly via latent cooling. This surface wind–enhanced negative surface heat flux anomaly, which extends southwestward across the basin and penetrates into the tropics, resembles the Pacific meridional mode pattern (PMM; Chiang and Vimont 2004; Amaya 2019).

It should be emphasized that our wind stress overriding protocol only specifies the mechanical wind stress felt by the

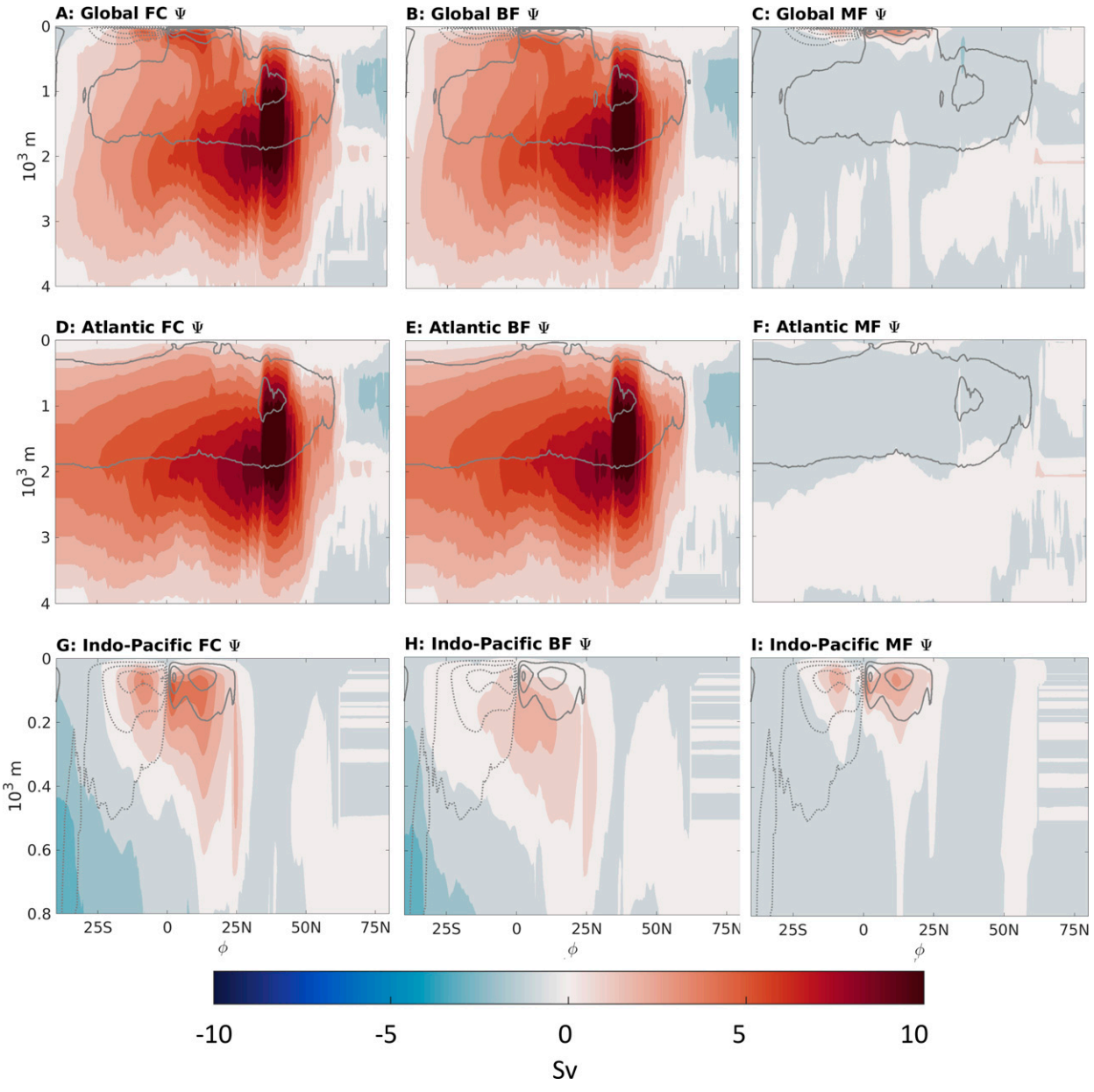

FIG. 6. (top) Global meridional overturning circulation (MOC; Ψ) response for (a) FC, (b) BF, and (c) MF, shown as colored contours with 1-Sv spacing. The time average of the unperturbed MOC in the control climate, Clim1, is given as gray contours of 10 Sv. (middle) Atlantic meridional overturning circulation (AMOC) response for (d) FC, (e) BF, and (f) MF as colored contours of 1 Sv. The time average of the unperturbed Clim1 AMOC response is given as gray contours of 10 Sv. (bottom) Indo-Pacific meridional overturning circulation response for (g) FC, (h) BF, and (i) MF as colored contours of 1 Sv. The time average of the unperturbed Clim1 Indo-Pacific MOC response is given as gray contours of 10 Sv. Note the change in vertical scale between the top two rows and the bottom row.

ocean. As a result, CESM's wind can still contribute to changes in Q_{net} via wind-driven sensible and latent heating. Any effect caused by mechanical and thermodynamic wind effects being out of step is a decoupling effect. Comparison of Clim1 and Tau1S1 in Figs. S2j–l show that the decoupling effects in our protocol are generally negligible when zonally averaged. Although they are larger than the decoupling effects, the extratropical SST and Q_{net} MF responses in Fig. 7c are also smaller in magnitude than the FC and BF responses and nearly cancel out in the zonal average.

In the equatorial Indo-Pacific, strong zonally asymmetric patterns abound in FC. In particular, the FC SST patterns in the Indian Ocean suggest a negative phase of the Indian Ocean dipole (IOD), while patterns in the Pacific Ocean show an enhanced La Niña–like response to extratropical cooling. This agrees qualitatively with the response of other

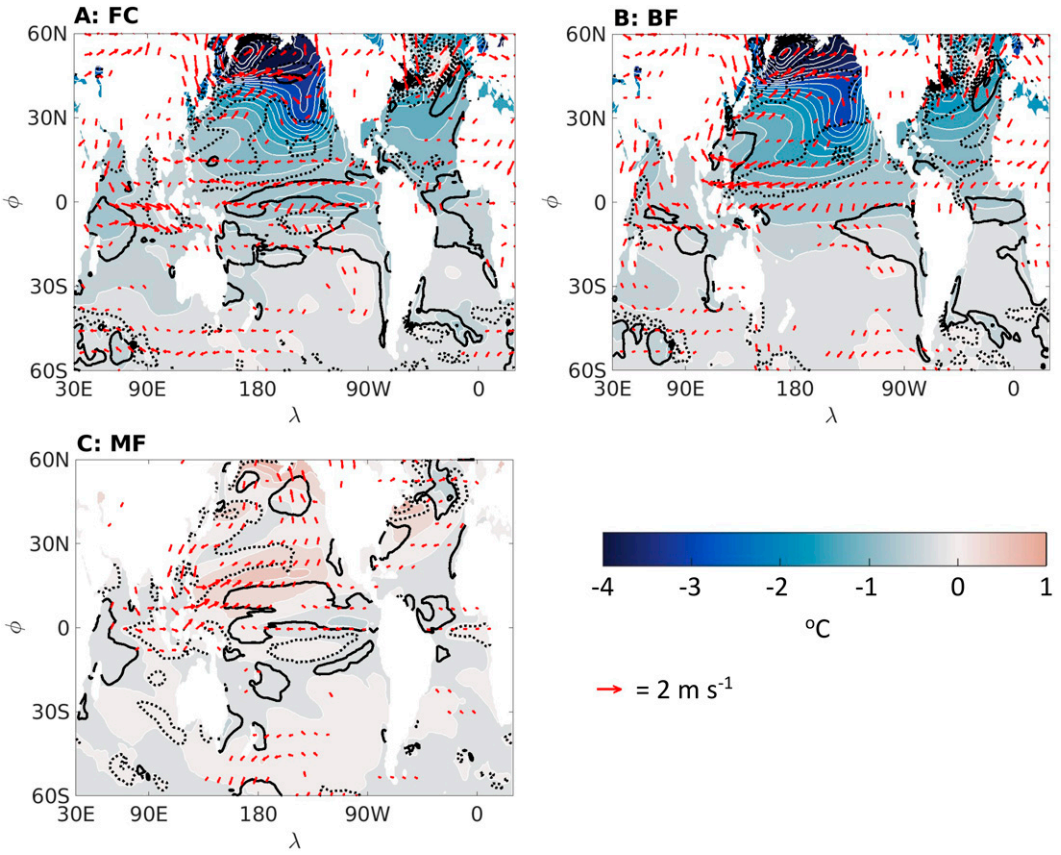

FIG. 7. (a) SST (colors and white contours), $Q_{net} > 0$ (solid black contours), $Q_{net} < 0$ (dotted black contours), and 850-hPa wind (arrows) for the FC response. SST contours are every 0.25°C, Q_{net} contours are every 12 W m^{-2} starting at ±3 W m^{-2}, and arrows with a magnitude smaller than ±0.2 m s^{-1} are zeroed out for visualization purposes. (b) SST, Q_{net}, and 850-hPa wind for the BF response, with colors, contours, and arrows as in (a). (c) SST, Q_{net}, and 850-hPa wind for the MF response, with colors, contours, and arrows as in (a).

ETINMIP-style NH extratropical TOA insolation reduction experiments, such as those of Kang et al. (2019), who present an ensemble mean of GCM responses, and Kang et al. (2020), who force a different GCM. Collectively, this La Niña pattern, most clear in cold tongue anomalies in the eastern equatorial Pacific, is created by both BF and MF together. BF provides a prominent, zonally symmetric background cooling of the equatorial Pacific and captures a PMM pattern that reaches the equator with anomalous northeasterly winds. Meanwhile, our MF case is uniquely useful for isolating the Bjerknes feedback because changes in wind stress drive the ocean response. We see that easterly trade wind anomalies shoal the eastern equatorial Pacific's thermocline and create a zonal asymmetry of a strengthened eastern cold tongue indicative of La Niña. This La Niña pattern and its associated cooling is likely responsible for the negative precipitation anomaly on the equator associated with MF in Fig. 2c.

That extratropical forcing can excite an ENSO-like event is not necessarily surprising. As we see in Fig. 7b, a PMM pattern extends southwestward across the NH subtropical Pacific into the tropics, propagated by the wind–evaporation–SST (WES) feedback (Xie and Philander 1994). These PMM events are known to be possible triggers for ENSO events by providing anomalous atmospheric forcing that can then excite a Bjerknes feedback (Vimont et al. 2003; Chang et al. 2007; Larson and Kirtman 2013, 2014; Lu et al. 2017; Pegion and Selman 2017; Ma et al. 2017; Amaya 2019). IOD patterns have also been associated with ENSO events (Annamalai et al. 2005) via equatorial waves. Several studies have also shown that high-latitude NH volcanic events and their subsequent stratospheric aerosol injection can generate ENSO responses in the tropical Pacific by shifting the ITCZ southward, weakening equatorial easterly trades, and warming the eastern equatorial Pacific through the Bjerknes feedback (Pausata et al. 2015, 2016; Stevenson et al. 2016).

b. *Partitioning of Indo-Pacific OHT*

Because there is no substantial deep convection in the North Pacific, there is no climatological buoyancy-forced deep Pacific MOC analogous to the AMOC (Talley et al. 2011). Hence the Indo-Pacific STCs have been pointed to as the primary cross-equatorial OHT pathway in the Indo-Pacific. While a strong AMOC response is expected given our NH

extratropical TOA forcing (e.g., YP19), the cross-equatorial OHT response in the Indo-Pacific is similar in magnitude to the Atlantic cross-equatorial OHT response: both basins contribute about 0.2 PW to the total cross-equatorial OHT (Figs. 5b,c).

Figure 5c shows that this FC response of Indo-Pacific cross-equatorial OHT is, surprisingly, also primarily a result of the BF response. The prevailing view, as suggested by GM17 and Green et al. (2019), is that changes in the trade winds cause substantial changes in the STCs which induce momentum-forced cross-equatorial heat transport. In Fig. 5c, we see that the cross-equatorial MF OHT response is slightly positive, which agrees qualitatively with GM17. However, compared with buoyancy forcing, the magnitude of momentum forcing in damping the response of the ITCZ by moving heat cross-equatorially is overstated by prior theories. While the MF response of the cross-equatorial OHT is larger in the Indo-Pacific than in the Atlantic, it still is only about a quarter of the size of the Indo-Pacific BF response. Although there is a clear latitudinal dependence to the MF response (BF and MF are roughly the same size near both 15°N and 10°S), the magnitude of cross-equatorial OHT is most important for understanding how the ocean damps ITCZ shifts. This leads to the central result of this study: buoyancy forcing drives the cross-equatorial OHT response to NH extratropical forcing in the Indo-Pacific. Momentum forcing plays a considerably smaller role.

The total Indo-Pacific MOC response presented in Fig. 6g is asymmetric about the equator, differing from the climatological STCs, which are more equatorially symmetric (gray contours in Figs. 6g–i). While the climatological STCs may be primarily momentum-forced (McCreary and Lu 1994; Liu 1994), the transient response of the STC is a combination of an anomalous, asymmetric, buoyancy-forced shallow MOC (Fig. 6h) and an even shallower, asymmetric, momentum-forced MOC (Fig. 6i), which somewhat resembles the canonical symmetric two-celled STC response suggested by studies such as GM17.

The BF anomalous MOC in Fig. 6h is unexpected and does not line up with previous understanding of Indo-Pacific OHT adjustment mechanisms. To ensure that it is indeed the anomalous shallow BF MOC in Fig. 6h that drives the anomalous cross-equatorial BF OHT in Fig. 5c, Fig. S7 shows the decomposition of cross-equatorial (average of 10°S–10°N) OHT outlined in Derivation S1 (see the online supplemental material). Most importantly, the dynamic response (i.e., the anomalous advection of the mean temperature; blue bars in Fig. S7), is the dominant component of the total cross-equatorial OHT response (black bars in Fig. S7) in nearly every scenario, including the case of the Indo-Pacific's anomalous BF cross-equatorial OHT (Fig. S7b).

Recent studies have highlighted the importance of the "inter-basin seesaw" (Sun et al. 2022) which exchanges heat between the Atlantic and Indo-Pacific on centennial timescales through a deep overturning circulation caused by wave adjustment (e.g., Garuba and Klinger 2016; Newsom and Thompson 2018; Holmes et al. 2019; Sun et al. 2020, 2022). Perhaps because of the short length of our simulations with respect to the deep ocean, we find no evidence of an anomalous cross-equatorial deep overturning circulation in the Indo-Pacific (not pictured). Because our cross-equatorial heat transport decomposition highlights dynamic changes as the driver of the anomalous BF OHT seen in Fig. 5c, we diagnose the anomalous shallow MOC in the BF response to be the main driver of the anomalous BF cross-equatorial OHT.

More broadly, this suggests that anomalous cross-equatorial heat transport occurs primarily due to dynamic changes, while thermodynamic and nonlinear terms are less important, a result mirrored in YP19. While several recent studies have suggested that passive, or thermodynamic, circulation drives patterns of ocean heat uptake in the case of global warming (e.g., Armour et al. 2016; Garuba and Klinger 2016, 2018; Newsom et al. 2020), in our case of hemispherically asymmetric NH extratropical forcing, this decomposition serves to emphasize the importance of dynamical adjustment in cross-equatorial OHT. It also underscores our interpretation in section 3d that the buoyancy-forced AMOC change drives Atlantic OHT (Fig. S7b).

c. *Thermohaline drivers of Indo-Pacific buoyancy-forced shallow MOC*

As suggested by the different vertical scales between the deep Atlantic buoyancy-forced response in Fig. 6e and the shallow Indo-Pacific buoyancy-forced response in Fig. 6h, the Indo-Pacific buoyancy-forced MOC response is governed by different dynamics than the AMOC and not simply a deep convection driven Indo-Pacific version of the AMOC. Nevertheless, our BF experiment explicitly demonstrates that buoyancy forcing from thermohaline drivers spur both the AMOC and our Indo-Pacific shallow MOC contained within the STCs. To hypothesize the physical drivers of this unexpected BF shallow MOC, we analyze Indo-Pacific density and surface buoyancy forcing responses, which point us toward specific physical processes.

Noting that subtropical gyre thermocline waters most closely resemble late winter mixed-layer waters, Stommel (1979) proposed that the seasonal cycle of the mixed layer acts as a "demon" that controls which waters enter the thermocline. Figures 8a and 8b plot tropical and NH extratropical Indo-Pacific surface potential density $\sigma_0(\lambda, \phi)$ from January through March (JFM) for FC and BF. As expected, the late winter surface potential density responses are quite similar. Although σ_0 increases throughout the NH Pacific in FC and BF, the most obvious feature is the positive bull's-eye-like σ_0 anomaly in the eastern subtropical Pacific around 30°N. Zonal-mean profiles of annual-mean Indo-Pacific FC and BF σ_0 responses in Figs. 8c and 8d largely follow the surface σ_0 responses in Figs. 8a and 8b: deep σ_0 perturbations directly underlie the positive eastern subtropical Pacific surface bull's-eye and extend vertically well into the thermocline.

The fact that the anomalous FC and BF MOCs cross isopycnals in Figs. 8c and 8d indicates a diapycnal anomaly,

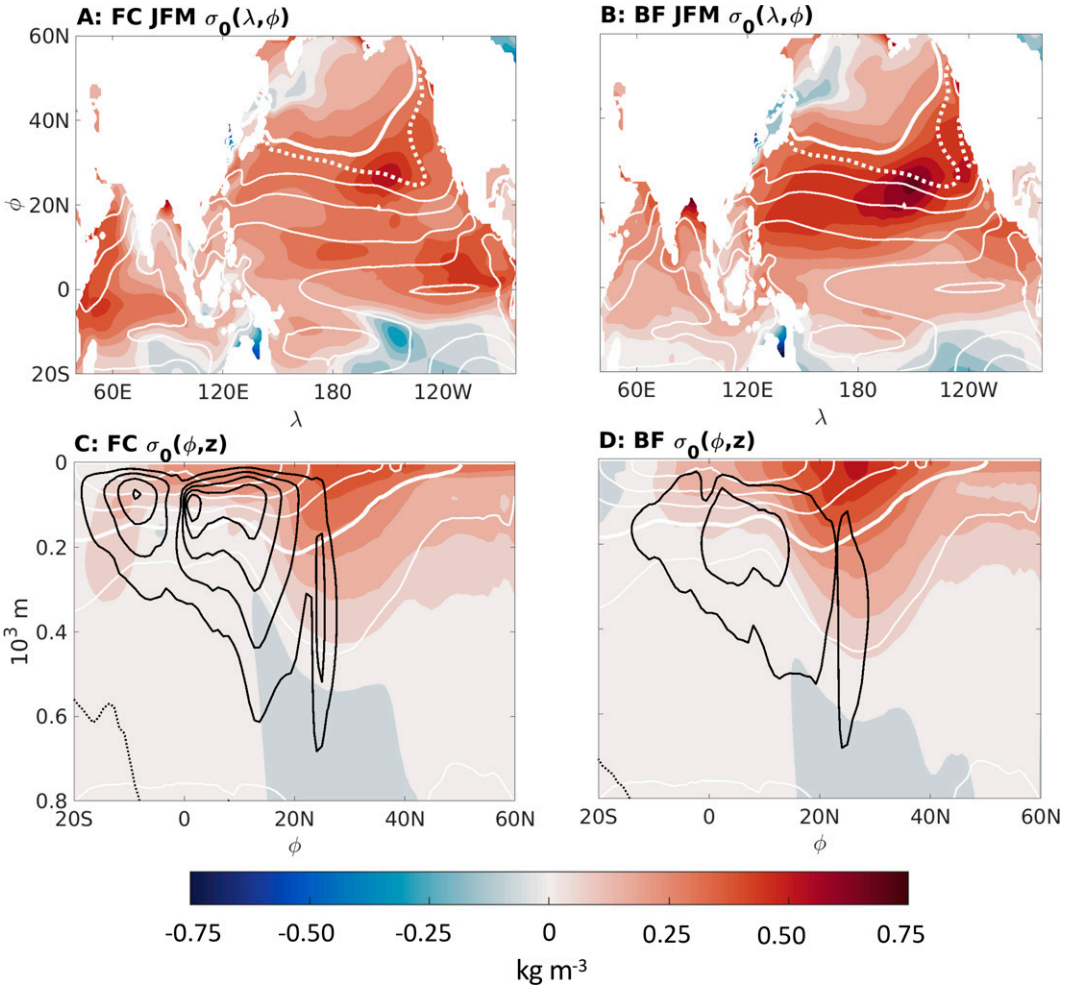

FIG. 8. (top) January–March (JFM) surface potential density, σ_0, response for (a) FC and (b) BF as colored contours every 0.075 kg m^{-3}. (bottom) Indo-Pacific annual-mean, zonal-mean σ_0 response for (c) FC and (d) BF as colored contours every 0.075 kg m^{-3} overlain with the Indo-Pacific MOC response in Figs. 6g and 6h as black contours of 1 Sv. Solid white contours in (a) and (b) are the JFM average of the unperturbed σ_0 isopycnals in Clim1 every 1 kg m^{-3} from 20 to 25 kg m^{-3}. Note that $\sigma_0 = 25$ kg m^{-3} in Clim1 is plotted as a thick, solid contour and $\sigma_0 = 25$ kg m^{-3} in Clim2 in (a) and Tau1S2 in (b) is plotted as a thick, dotted contour. White contours in (c) and (d) are the annual-mean unperturbed σ_0 isopycnals in Clim1 every 1 kg m^{-3} from 22 to 27 kg m^{-3} with $\sigma_0 = 25$ kg m^{-3} thickened.

which can help explain our anomalous BF MOC. In a direct analog to the Eulerian-mean MOC Ψ, defined in Eq. (7) on vertical coordinates, following Sun et al. (2018) we define the Eulerian-mean MOC in density coordinates as

$$\Psi_{\sigma 0}(\phi,\ \sigma_0) = a\cos\phi\int_{z_{\rm bot}}^{0}\int_{\lambda_w}^{\lambda_e} v(\lambda,\phi,z)\mathcal{H}[\sigma_0'(\lambda,\ \phi,\ z) - \sigma_0]\ d\lambda\, dz. \tag{8}$$

In Eq. (8), $z_{\rm bot}$ is the ocean bottom, $\mathcal{H}$ is the Heaviside step function, $\sigma_0'(\lambda,\ \phi,\ z)$ is the surface potential density field, and σ_0 is the vector of surface potential densities we integrate over. Figures 9a–c respectively present anomalous $\Psi_{\sigma 0}$ for FC, BF, and MF. While it can be difficult to definitively interpret $\Psi_{\sigma 0}$ differences if the MOC is not in steady state, all three transient overturning responses presented here cross isopycnals in some capacity. The FC and BF overturning responses show an increased overturning at densities below the climatological STCs. Focusing in particular on the NH lobe of the FC and BF $\Psi_{\sigma 0}$ responses, we see a large diapycnal overturning extending from $\sigma_0 = 22$–24.5 kg m^{-3}. This anomaly represents the shift of the STC to a higher density class, which would be expected from surface cooling. We observe a decrease in stratification, the vertical gradient of density, at depth, and, because CESM's vertical diffusivity depends on stratification, this represents a potential enhancement of parameterized vertical diapycnal mixing. We conclude that changes in interior diapycnal mixing as a result of evolving stratification are partially responsible for the anomalous BF MOC in the Indo-Pacific.

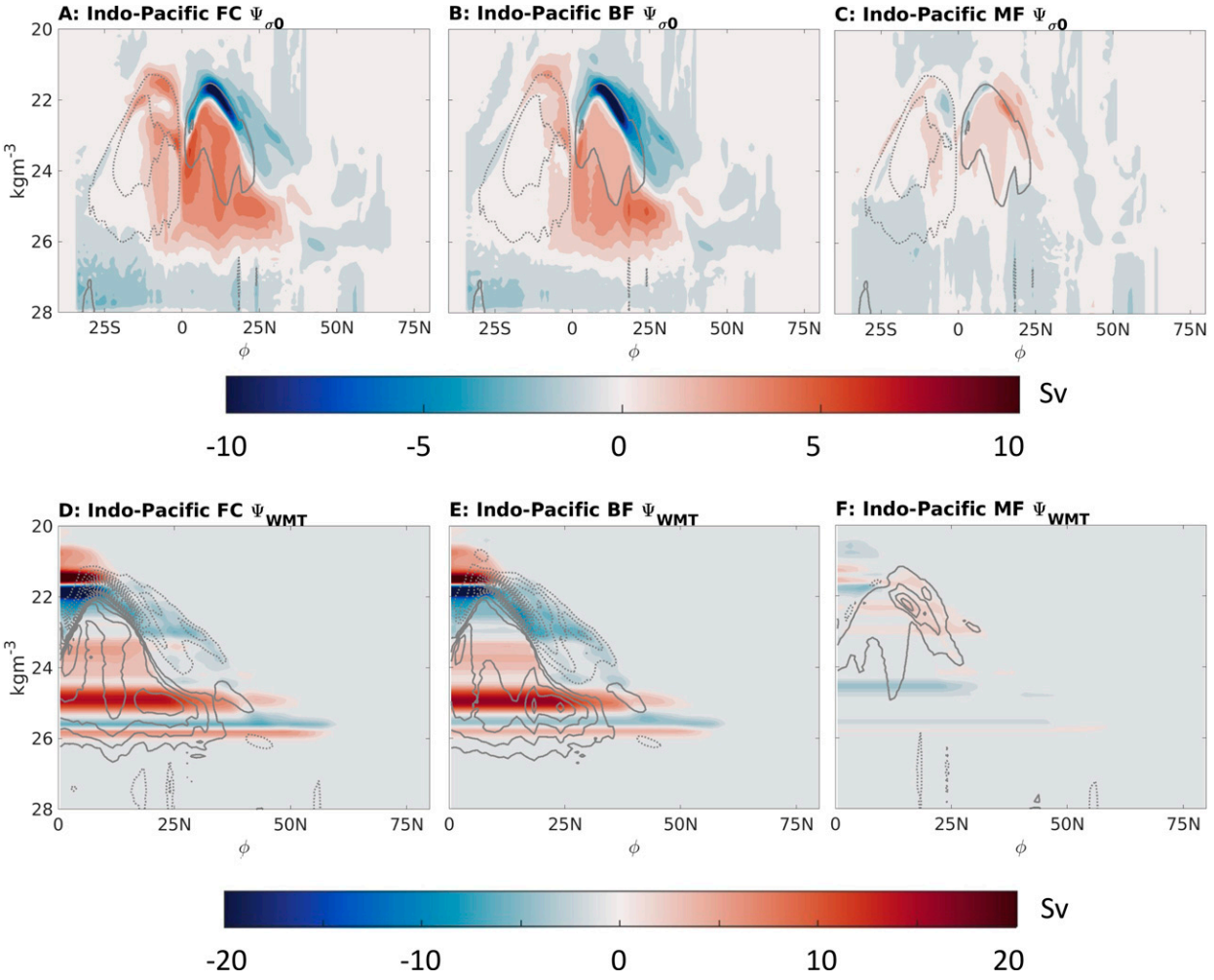

FIG. 9. (top) Indo-Pacific $\Psi_{\sigma 0}$ response for (a) FC, (b) BF, and (c) MF as colored contours every 1 Sv. The time average of the unperturbed Indo-Pacific $\Psi_{\sigma 0}$ in the control climate, Clim1, is given as gray contours of 10 Sv. (bottom) Indo-Pacific Ψ_{WMT} response for (d) FC, (e) BF, and (f) MF as colored contours every 1 Sv. The corresponding Indo-Pacific $\Psi_{\sigma 0}$ response (colors from top row) is overlain as gray contours of 1 Sv.

Interestingly, at $\sigma_0 = 24.5$–25.5 kg m^{-3} there is a stronger and more isopycnal anomalous overturning extending from the equator to around 30°N. To explain this isopycnal aspect of the anomalous BF MOC, we consider how surface buoyancy forcing influences the anomalous MOC by diagnosing surface water mass transformations in the Indo-Pacific (Walin 1982; Speer and Tziperman 1992). Following Newsom et al. (2016), we define surface buoyancy flux Q_B as

$$Q_B(\lambda, \phi) = -\frac{\alpha}{C_p} Q_{\mathrm{net}}(\lambda, \phi) - \frac{\rho_0}{\rho_{\mathrm{FW}}} \beta S_0 Q_{\mathrm{FW}}(\lambda, \phi), \tag{9}$$

where α and β are the coefficients of thermal expansion and saline contraction, ρ_{FW} is the density of freshwater, S_0 is a reference salinity, and Q_{FW} is the surface freshwater flux, reported in CESM as the history field "SFWF." Per Eq. (9), Q_B is a linear sum of net surface heat and net surface freshwater flux in units of kg m^{-2} s^{-1}. Figures S8a and S8d show FC's and BF's Q_B fields for the Indo-Pacific. In this surface water mass transformation framework, we can then define the surface-forced overturning streamfunction Ψ_{WMT} (Marsh 2000; Grist et al. 2009; Oldenburg et al. 2021) as

$$\Psi_{\mathrm{WMT}}(\phi, \sigma_0) = -a^2 \cos\phi \frac{\partial}{\partial \sigma_0} \int\int_{\phi' > \phi, \sigma_0' > \sigma_0} Q_B(\lambda, \phi)\, d\lambda\, d\phi, \tag{10}$$

where ϕ' and σ_0' are dummy integration variables for latitude and potential density. In this framework, $\Psi_{\sigma 0}$ and Ψ_{WMT} are directly comparable and explain how much of $\Psi_{\sigma 0}$ is attributable to water mass transformation with the residual attributed to mixing, which is not accounted for in this framework. Color fill in Figs. 9d–f presents the Ψ_{WMT} response for the FC, BF, and MF responses and they are overlain with $\Psi_{\sigma 0}$ contours for each respective case for direct comparison. While there is an obvious bias on the order of 10 Sv in Ψ_{WMT} compared to

$\Psi_{\sigma 0}$, substantial discrepancies have been found between surface-forced MOC and total MOC in prior studies and Ψ_{WMT} estimates are typically stronger than $\Psi_{\sigma 0}$ (Grist et al. 2009; Oldenburg et al. 2021). Nevertheless, we find this to be a useful qualitative diagnostic framework. It suggests that the more isopycnal overturning along $\sigma_0 = 24.5$–25.5 kg m^{-3} in this anomalous MOC is strongly influenced by surface buoyancy forcing (Fig. S8).

While decreased stratification and increased surface buoyancy forcing help to dynamically explain the anomalous BF MOC in the Indo-Pacific, a few major big-picture questions remain, such as why the BF MOC is located where it is and how thermohaline anomalies are communicated from the high-latitude NH region where the insolation perturbation is applied into the tropics and across the equator.

5. Discussion

a. Low cloud feedback off the California coast

Whereas the insolation is reduced from 45° to 65°N, the maximum density anomaly in the Pacific occurs 3000 km away at 30°N (Figs. 8a,b). Here we consider how the low cloud feedback may help to explain the spatial disconnect between the insolation perturbation and the maximum density anomaly.

The low cloud feedback is a positive feedback on the climate system (e.g., Norris and Leovy 1994; Norris et al. 1998; Clement et al. 2009; Wood 2012; Gettelman and Sherwood 2016; Sherwood et al. 2020; Yang et al. 2022). In the case of reduced NH insolation, the strengthened subtropical high pressure system in the central northern Pacific leads to strengthened anticyclonic geostrophic near-surface winds (Fig. 7b). These winds contribute to SST cooling along the coast of California in the eastern subtropical Pacific via sensible and latent heat flux changes and they contribute to the coastal cool tongue extending southward seen in Figs. 7a and 7b.

These wind-cooled SSTs extend southward into the eastern subtropical Pacific's marine stratiform deck, a low-cloud-dominated regime. The marine stratiform regime is strong on the eastern flank of subtropical high pressure zones as cold advection within the atmospheric boundary layer from geostrophic northerly winds cool SST and drive westward Ekman transport (Talley et al. 2011; Wood 2012). Combined with Hadley cell subsidence, which creates a strong inversion, these regions are ripe with low clouds. In the case of NH cooling, the low cloud positive feedback works to amplify any negative temperature anomalies introduced by anomalous winds by increasing low cloud fraction, blocking incoming shortwave, and creating denser waters beneath the marine stratiform deck. Yang et al. (2022) show that the low cloud feedback in the northeast Pacific cloud deck is even locally strong enough to offset evaporative damping of SST.

Figure S9 shows the surface SW and low cloud fraction anomalies. Because low clouds block insolation from reaching the ocean surface, a substantial increase in low cloud fraction directly coincides with the reduction in SW. This low cloud bull's-eye in FC and BF helps to regionally amplify the density anomaly shown in Figs. 8a and 8b.

b. Communication of anomalies via ventilated thermocline

This raises the question of how these density anomalies are communicated from the eastern subtropical Pacific to the tropics and ultimately across the equator. In early work describing the physical basis of the STCs, McCreary and Lu (1994) and Liu (1994) used the ventilated thermocline model of the subtropical gyre first proposed by Luyten et al. (1983) to connect tropical and subtropical variability. In particular, by communicating anomalies along streamlines to the western side of the basin, the subtropical eastern Pacific provides a boundary condition for the tropics. These anomalies are communicated via mean advection and westward propagating Rossby waves (McCreary and Lu 1994; Liu 1994; Qiu et al. 1997; Huang and Pedlosky 1999; Liu 1999; Nonaka et al. 2000).

Studies that investigated buoyancy forcing of the STC are particularly relevant for the present discussion (Huang and Pedlosky 1999; Shin and Liu 2000; Thompson and Ladd 2004). In particular, Huang and Pedlosky (1999) analytically show that cooling leads to equatorward isopycnal outcrop shifts, which induces baroclinicity in the upper and lower thermocline and excites westward-propagating baroclinic Rossby waves. Figures 8a and 8b clearly show this equatorward isopycnal outcrop shift, as positive density perturbations lead the $\sigma_0 = 25$ kg m^{-3} outcrop to shift about 10° southward compared to the climatology. Carried to the western basin via mean advection and baroclinic Rossby waves, these anomalies can be communicated to the equator via mean flow of the western boundary current or coastal Kelvin waves (Shin and Liu 2000). We leave the details of this buoyancy-forced cross-equatorial adjustment to future work.

c. Model diversity

The results presented here suggest that the buoyancy-forced Indo-Pacific shallow MOC changes shown in Fig. 6h result from density anomalies in the eastern subtropical Pacific amplified by the low cloud positive feedback. Because this low cloud response stands out in all three of our ensemble members, and because it is also seen in the results of YP19 (their Fig. 13) despite a different forcing scheme, this eastern subtropical Pacific low cloud feedback may be a robust response in CESM. However, the strength of this feedback is likely to depend on the choice of model, with the marine stratiform regimes potentially responding differently in different GCMs. This suggests that the details of the buoyancy-forced response to the same NH TOA radiative forcing perturbation may vary among GCMs.

d. Ocean heat transport response driven primarily by buoyancy forcing

The buoyancy-forced asymmetric shallow Indo-Pacific MOC shown in Fig. 6h is a result at odds with expectations based on previous studies. Although GM17 suggested that the

transient response of the Indo-Pacific MOC to interhemispheric Q_{net} changes arises as a linear combination of a symmetric STC change and an asymmetric cross-equatorial cell change, both of these cells are theorized to be momentum-forced. In contrast to this, our results suggest that the asymmetric OHT response that dominates the total cross-equatorial response is in fact buoyancy-forced. Further, the weaker momentum-forced OHT response of the Indo-Pacific MOC is also asymmetric. Strikingly, the small cross-equatorial influence of MF in the Indo-Pacific and its negligible influence in the Atlantic is at odds with preexisting hypotheses regarding mechanically driven changes in the STCs from changes in trade winds as a damping mechanism for ITCZ shifts (Held 2001; Schneider et al. 2014; Kay et al. 2016; Green and Marshall 2017; Schneider 2017; Green et al. 2019). Varying the time averaging window does not seem to change this conclusion (see Fig. S10). While we have focused on cross-equatorial OHT and its resulting ITCZ impacts in this study, it is worth pointing out that MF does seem to be a major player in the Indo-Pacific in carrying heat from the northern tropics to the subtropical cooling region (Fig. 5c).

Liu et al. (2021) heat the surface of the Southern Ocean and implement climatological wind stress overriding, which provides results that are complementary to this study. After overriding the wind stress, a deep buoyancy-forced clockwise cell develops that extends from the Southern Ocean into the tropics in both the Indo-Pacific and Atlantic basins (see their Fig. 8). This Southern Ocean buoyancy-forced cell occurs in the absence of an AMOC response such that the Indo-Pacific drives more OHT than the Atlantic as a result of its width. As discussed in YP19, the transient AMOC response is highly sensitive to forcing latitude, so our strong AMOC response and Liu et al.'s (2021) lack thereof is not necessarily surprising given that we forced different latitudes. Rather, the fact that Liu et al. (2021) heat the Southern Ocean surface and find a deep buoyancy-forced MOC in both the Atlantic and the Indo-Pacific, whereas we reduce the energy input in the NH TOA and observe a strong AMOC response and a mostly buoyancy-forced shallow MOC in the Indo-Pacific, suggests that the ocean's transient adjustment to interhemispheric asymmetric Q_{net} forcing is sensitive to forcing type and location.

Of course, this adds yet another layer of complexity to the question of how exactly the ocean dynamically adjusts and damps ITCZ shifts in the face of interhemispheric Q_{net} asymmetry. Much as YP19 see that radiative forcing applied at different latitudes induces different AMOC responses, our results suggest that while buoyancy forcing is the preferred mechanism for cross-equatorial heat transport compared to momentum forcing, buoyancy forcing can come in different forms that will vary the OHT response. Rather than an idealized theory of the ocean damping ITCZ shifts via buoyancy forcing in the Atlantic and momentum forcing in the Indo-Pacific, our results suggest that the ocean can work in more complicated ways than often assumed in zonal-mean energy transport theory to smooth out energetic gradients in the ocean–atmosphere coupled system.

6. Conclusions

We have presented results from a set of GCM simulations that utilize wind stress overriding and NH TOA insolation reduction. Our systematic experimental design has allowed us to isolate and attribute the effects of thermohaline changes alone and wind stress changes alone with a specific focus on the ocean's cross-equatorial heat transport. In particular, we find that buoyancy forcing dominates the total OHT response, with negligible momentum forcing in the Atlantic and smaller than expected momentum forcing in the Indo-Pacific. The shallow subtropical overturning circulation in the Indo-Pacific does transport heat northward but this OHT comprises a stronger and deeper asymmetric buoyancy-forced cell and a weaker asymmetric momentum-forced cell. We suggest that this shallow Indo-Pacific MOC is driven by subtropical thermohaline anomalies created by ocean–atmosphere interactions, amplified by the low cloud feedback off the coast of California, and then communicated cross-equatorially via the ventilated thermocline.

The central result of this study is that buoyancy forcing plays a dominant role in the transient adjustment of the ocean to NH extratropical forcing perturbations in each basin. While the wind stress-forced component of the STCs do in fact transport heat northward in the Indo-Pacific, the magnitude of the response is not as large as prior studies have theorized (Held 2001; Schneider et al. 2014; Kay et al. 2016; Schneider 2017; Green and Marshall 2017; Green et al. 2019). Rather, the present study fits into a group of studies that share a recognition of the importance of the buoyancy-forced response of transient ocean adjustment (e.g., Shin and Liu 2000; Hogg 2010; Wang et al. 2015; Gjermundsen et al. 2018; Hogg and Gayen 2020; Shi et al. 2020). On a more practical level, this study suggests that the buoyancy-forced response to energy perturbations is basin-specific, such that a more complete theory of the ocean's effect on ITCZ migrations must consider the forcing type and meridional location.

Acknowledgments. This work was supported by National Science Foundation (NSF) grants 2048590 and 1934392. We thank UCAR and NSF for providing the graduate student allocation of core hours on Cheyenne that this research used and the ETINMIP group for making their NEXT experimental code available. Without implying their endorsement, we thank Sungduk Yu, Shantong Sun, Yen-Ting Hwang, Wei Liu, Mark England, and Pengcheng Zhang for helpful discussions and suggestions. We also thank Dr. Isaac Held and three anonymous reviewers for their thoughtful and constructive feedback, which greatly improved this manuscript. In particular, Reviewer 3 suggested the water mass transformation analysis of Fig. 9. The authors declare no conflicts of interest.

Data availability statement. The data used throughout this study are publically available through the University of California, San Diego library digital collections: https://doi.org/10.6075/J05X294K. The source code developed to override wind stress in CESM1.2 is available on MTL's Github page and at

https://doi.org/10.6075/J09P31TF. The ETINMIP TOA insolation reduction code is available upon request from Kang et al. (2019).

APPENDIX

Relating Q_{net} to OHT

Following Liu et al. (2018) and Hu et al. (2020), we consider the heat budget of each full-depth column of the ocean. The total heating Q_{net} can be written as the sum of sensible heat flux (SHF), latent heat flux (LHF), and both shortwave (SW) and longwave (LW) radiative fluxes,

$$Q_{\text{net}} = \text{SHF} + \text{LHF} + \text{SW} + \text{LW}. \tag{A1}$$

Here all quantities are defined as positive downward in units of W m^{-2}. Note that the term we call Q_{net} is reported in CESM as the ocean history field "SHF," which stands for surface heat flux, but in the present study we use "SHF" to refer to sensible heat flux.

We define ocean heat content (OHC) as a vertically integrated quantity,

$$\text{OHC} = \rho_0 C_p \int_{-H}^{0} \theta \, dz, \tag{A2}$$

where OHC is the product of the seawater density, which we take to be constant at $\rho_0 = 1026$ kg m^{-3}, the specific heat capacity of seawater $C_p = 3996$ J kg^{-1} °C^{-1}, and the potential temperature θ (°C), integrated from the sea floor ($z = -H$) to the sea surface ($z = 0$).

Changes in Q_{net} are associated with changes in the ocean column's heat storage (OHS), the time tendency of OHC,

$$\text{OHS} = \frac{\partial}{\partial t}\text{OHC}, \tag{A3}$$

and changes in the ocean column's horizontal heat flux divergence (OHD), which includes the effects of both advection and parameterized eddy diffusion. Approximating the ocean to be incompressible ($\nabla \cdot \mathbf{u}_T = 0$), this can be written as

$$\begin{aligned} \text{OHD} &= \rho_0 C_p \int_{-H}^{0} [\nabla \cdot (\mathbf{u}_T \, \theta) + D] \, dz \\ &= \rho_0 C_p \int_{-H}^{0} (\mathbf{u}_T \cdot \nabla\theta + D) \, dz. \end{aligned} \tag{A4}$$

Here, D is the divergence of isoneutral diffusive flux parameterized in CESM with the Redi scheme to simulate subgrid-scale diffusive processes including geostrophic eddies, and $\mathbf{u}_T$ is the total three-dimensional ocean velocity vector with u_T, v_T, and w_T representing the zonal, meridional, and vertical velocity components, respectively.

As such, changes in Q_{net} are associated with changes in OHS or OHD, both of which are vertically integrated quantities:

$$Q_{\text{net}} = \text{OHS} + \text{OHD}. \tag{A5}$$

The meridional ocean heat transport (OHT) at a given latitude ϕ can be written as the meridional integral from ϕ to the North Pole ($\phi = \pi/2$) of OHD integrated zonally across longitudes λ from the western edge of a basin ($\lambda = \lambda_w$) to the eastern edge of a basin ($\lambda = \lambda_e$):

$$\text{OHT} = -\int_{\phi}^{\pi/2} a^2 \cos\phi' \int_{\lambda_w}^{\lambda_e} \text{OHD} \, d\lambda \, d\phi'. \tag{A6}$$

Here, $a = 6371$ km is the radius of Earth, and a negative sign is included for the convention that positive OHT represents northward heat transport.

REFERENCES

Amaya, D. J., 2019: The Pacific meridional mode and ENSO: A review. *Curr. Climate Change Rep.*, **5**, 296–307, https://doi.org/10.1007/s40641-019-00142-x.

——, N. Siler, S.-P. Xie, and A. J. Miller, 2018: The interplay of internal and forced modes of Hadley cell expansion: Lessons from the global warming hiatus. *Climate Dyn.*, **51**, 305–319, https://doi.org/10.1007/s00382-017-3921-5.

Annamalai, H., S. Xie, J. McCreary, and R. Murtugudde, 2005: Impact of Indian Ocean sea surface temperature on developing El Niño. *J. Climate*, **18**, 302–319, https://doi.org/10.1175/JCLI-3268.1.

Armour, K. C., J. Marshall, J. R. Scott, A. Donohoe, and E. R. Newsom, 2016: Southern Ocean warming delayed by circumpolar upwelling and equatorward transport. *Nat. Geosci.*, **9**, 549–554, https://doi.org/10.1038/ngeo2731.

Broccoli, A. J., K. A. Dahl, and R. J. Stouffer, 2006: Response of the ITCZ to Northern Hemisphere cooling. *Geophys. Res. Lett.*, **33**, L01702, https://doi.org/10.1029/2005GL024546.

Broecker, W. S., 1997: Thermohaline circulation, the Achilles heel of our climate system: Will man-made CO_2 upset the current balance? *Science*, **278**, 1582–1588, https://doi.org/10.1126/science.278.5343.1582.

——, 2003: Does the trigger for abrupt climate change reside in the ocean or in the atmosphere? *Science*, **300**, 1519–1522, https://doi.org/10.1126/science.1083797.

Buckley, M. W., and J. Marshall, 2016: Observations, inferences, and mechanisms of the Atlantic meridional overturning circulation: A review. *Rev. Geophys.*, **54**, 5–63, https://doi.org/10.1002/2015RG000493.

Chang, P., L. Zhang, R. Saravanan, D. J. Vimont, J. C. Chiang, L. Ji, H. Seidel, and M. K. Tippett, 2007: Pacific meridional mode and El Niño–Southern Oscillation. *Geophys. Res. Lett.*, **34**, L16608, https://doi.org/10.1029/2007GL030302.

Chiang, J. C., and D. J. Vimont, 2004: Analogous Pacific and Atlantic meridional modes of tropical atmosphere–ocean variability. *J. Climate*, **17**, 4143–4158, https://doi.org/10.1175/JCLI4953.1.

——, and C. M. Bitz, 2005: Influence of high latitude ice cover on the marine Intertropical Convergence Zone. *Climate Dyn.*, **25**, 477–496, https://doi.org/10.1007/s00382-005-0040-5.

——, M. Biasutti, and D. S. Battisti, 2003: Sensitivity of the Atlantic intertropical convergence zone to last glacial maximum boundary conditions. *Paleoceanography*, **18**, 1094, https://doi.org/10.1029/2003PA000916.

Clement, A. C., R. Burgman, and J. R. Norris, 2009: Observational and model evidence for positive low-level cloud feedback. *Science*, **325**, 460–464, https://doi.org/10.1126/science.1171255.

Craig, A., 2014: CPL7 user's guide (updated for CESM version 1.0.6). CESM, 24 pp., https://www.cesm.ucar.edu/models/cesm1.2/cpl7/doc/ug.pdf.

Czaja, A., and J. Marshall, 2006: The partitioning of poleward heat transport between the atmosphere and ocean. *J. Atmos. Sci.*, **63**, 1498–1511, https://doi.org/10.1175/JAS3695.1.

Deser, C., and Coauthors, 2020: Isolating the evolving contributions of anthropogenic aerosols and greenhouse gases: A new CESM1 large ensemble community resource. *J. Climate*, **33**, 7835–7858, https://doi.org/10.1175/JCLI-D-20-0123.1.

Döös, K., and J. Nilsson, 2011: Analysis of the meridional energy transport by atmospheric overturning circulations. *J. Atmos. Sci.*, **68**, 1806–1820, https://doi.org/10.1175/2010JAS3493.1.

Eisenman, I., C. M. Bitz, and E. Tziperman, 2009: Rain driven by receding ice sheets as a cause of past climate change. *Paleoceanography*, **24**, PA4209, https://doi.org/10.1029/2009PA001778.

Forster, P., and Coauthors, 2021: The Earth's energy budget, climate feedbacks, and climate sensitivity. *Climate Change 2021: The Physical Science Basis*, V. Masson-Delmott et al., Eds., Cambridge University Press 923–1054, https://doi.org/10.1017/9781009157896.009.

Frierson, D. M., and Coauthors, 2013: Contribution of ocean overturning circulation to tropical rainfall peak in the Northern Hemisphere. *Nat. Geosci.*, **6**, 940–944, https://doi.org/10.1038/ngeo1987.

Fučkar, N. S., S.-P. Xie, R. Farneti, E. A. Maroon, and D. M. Frierson, 2013: Influence of the extratropical ocean circulation on the intertropical convergence zone in an idealized coupled general circulation model. *J. Climate*, **26**, 4612–4629, https://doi.org/10.1175/JCLI-D-12-00294.1.

Ganachaud, A., and C. Wunsch, 2003: Large-scale ocean heat and freshwater transports during the World Ocean Circulation Experiment. *J. Climate*, **16**, 696–705, https://doi.org/10.1175/1520-0442(2003)016<0696:LSOHAF>2.0.CO;2.

Garuba, O. A., and B. A. Klinger, 2016: Ocean heat uptake and interbasin transport of the passive and redistributive components of surface heating. *J. Climate*, **29**, 7507–7527, https://doi.org/10.1175/JCLI-D-16-0138.1.

——, and ——, 2018: The role of individual surface flux components in the passive and active ocean heat uptake. *J. Climate*, **31**, 6157–6173, https://doi.org/10.1175/JCLI-D-17-0452.1.

Gettelman, A., and S. Sherwood, 2016: Processes responsible for cloud feedback. *Curr. Climate Change Rep.*, **2**, 179–189, https://doi.org/10.1007/s40641-016-0052-8.

Gjermundsen, A., J. H. LaCasce, and L. Denstad, 2018: The thermally driven ocean circulation with realistic bathymetry. *J. Phys. Oceanogr.*, **48**, 647–665, https://doi.org/10.1175/JPO-D-17-0147.1.

Green, B., and J. Marshall, 2017: Coupling of trade winds with ocean circulation damps ITCZ shifts. *J. Climate*, **30**, 4395–4411, https://doi.org/10.1175/JCLI-D-16-0818.1.

——, ——, and J.-M. Campin, 2019: The 'sticky' ITCZ: Ocean-moderated ITCZ shifts. *Climate Dyn.*, **53** (1), 1–19, https://doi.org/10.1007/s00382-019-04623-5.

Gregory, J. M., and Coauthors, 2016: The Flux-Anomaly-Forced Model Intercomparison Project (FAFMIP) contribution to CMIP6: Investigation of sea-level and ocean climate change in response to CO_2 forcing. *Geosci. Model Dev.*, **9**, 3993–4017, https://doi.org/10.5194/gmd-9-3993-2016.

Grist, J. P., R. Marsh, and S. A. Josey, 2009: On the relationship between the North Atlantic meridional overturning circulation and the surface-forced overturning streamfunction. *J. Climate*, **22**, 4989–5002, https://doi.org/10.1175/2009JCLI2574.1.

Hawcroft, M., J. M. Haywood, M. Collins, A. Jones, A. C. Jones, and G. Stephens, 2017: Southern Ocean albedo, inter-hemispheric energy transports and the double ITCZ: Global impacts of biases in a coupled model. *Climate Dyn.*, **48**, 2279–2295, https://doi.org/10.1007/s00382-016-3205-5.

——, ——, ——, and ——, 2018: The contrasting climate response to tropical and extratropical energy perturbations. *Climate Dyn.*, **51**, 3231–3249, https://doi.org/10.1007/s00382-018-4076-8.

He, C., Z. Liu, and A. Hu, 2019: The transient response of atmospheric and oceanic heat transports to anthropogenic warming. *Nat. Climate Change*, **9**, 222–226, https://doi.org/10.1038/s41558-018-0387-3.

Held, I. M., 2001: The partitioning of the poleward energy transport between the tropical ocean and atmosphere. *J. Atmos. Sci.*, **58**, 943–948, https://doi.org/10.1175/1520-0469(2001)058<0943:TPOTPE>2.0.CO;2.

——, M. Winton, K. Takahashi, T. Delworth, F. Zeng, and G. K. Vallis, 2010: Probing the fast and slow components of global warming by returning abruptly to preindustrial forcing. *J. Climate*, **23**, 2418–2427, https://doi.org/10.1175/2009JCLI3466.1.

Hogg, A. M., 2010: An Antarctic Circumpolar Current driven by surface buoyancy forcing. *Geophys. Res. Lett.*, **37**, L23601, https://doi.org/10.1029/2010GL044777.

——, and B. Gayen, 2020: Ocean gyres driven by surface buoyancy forcing. *Geophys. Res. Lett.*, **47**, e2020GL088539, https://doi.org/10.1029/2020GL088539.

Holland, M. M., D. A. Bailey, B. P. Briegleb, B. Light, and E. Hunke, 2012: Improved sea ice shortwave radiation physics in CCSM4: The impact of melt ponds and aerosols on Arctic sea ice. *J. Climate*, **25**, 1413–1430, https://doi.org/10.1175/JCLI-D-11-00078.1.

Holmes, R. M., J. D. Zika, R. Ferrari, A. F. Thompson, E. R. Newsom, and M. H. England, 2019: Atlantic Ocean heat transport enabled by Indo-Pacific heat uptake and mixing. *Geophys. Res. Lett.*, **46**, 13 939–13 949, https://doi.org/10.1029/2019GL085160.

Hu, S., S.-P. Xie, and W. Liu, 2020: Global pattern formation of net ocean surface heat flux response to greenhouse warming. *J. Climate*, **33**, 7503–7522, https://doi.org/10.1175/JCLI-D-19-0642.1.

Huang, R. X., and J. Pedlosky, 1999: Climate variability inferred from a layered model of the ventilated thermocline. *J. Phys. Oceanogr.*, **29**, 779–790, https://doi.org/10.1175/1520-0485(1999)029<0779:CVIFAL>2.0.CO;2.

Hurrell, J. W., and Coauthors, 2013: The Community Earth System Model: A framework for collaborative research. *Bull. Amer. Meteor. Soc.*, **94**, 1339–1360, https://doi.org/10.1175/BAMS-D-12-00121.1.

Hwang, Y.-T., H.-Y. Tseng, K.-C. Li, S. M. Kang, Y.-J. Chen, and J. C. Chiang, 2021: Relative roles of energy and momentum fluxes in the tropical response to extratropical thermal forcing. *J. Climate*, **34**, 3771–3786, https://doi.org/10.1175/JCLI-D-20-0151.1.

Johnson, H. L., P. Cessi, D. P. Marshall, F. Schloesser, and M. A. Spall, 2019: Recent contributions of theory to our understanding of the Atlantic meridional overturning circulation. *J. Geophys. Res. Oceans*, **124**, 5376–5399, https://doi.org/10.1029/2019JC015330.

Kang, S. M., I. M. Held, D. M. Frierson, and M. Zhao, 2008: The response of the ITCZ to extratropical thermal forcing: Idealized slab-ocean experiments with a GCM. *J. Climate*, **21**, 3521–3532, https://doi.org/10.1175/2007JCLI2146.1.

——, D. M. Frierson, and I. M. Held, 2009: The tropical response to extratropical thermal forcing in an idealized GCM: The importance of radiative feedbacks and convective parameterization.

J. Atmos. Sci., **66**, 2812–2827, https://doi.org/10.1175/2009JAS2924.1.

——, Y. Shin, and S.-P. Xie, 2018: Extratropical forcing and tropical rainfall distribution: Energetics framework and ocean Ekman advection. *npj Climate Atmos. Sci.*, **1**, 20172, https://doi.org/10.1038/s41612-017-0004-6.

——, and Coauthors, 2019: Extratropical–Tropical Interaction Model Intercomparison Project (ETIN-MIP): Protocol and initial results. *Bull. Amer. Meteor. Soc.*, **100**, 2589–2606, https://doi.org/10.1175/BAMS-D-18-0301.1.

——, S.-P. Xie, Y. Shin, H. Kim, Y.-T. Hwang, M. F. Stuecker, B. Xiang, and M. Hawcroft, 2020: Walker circulation response to extratropical radiative forcing. *Sci. Adv.*, **6**, eabd3021, https://doi.org/10.1126/sciadv.abd3021.

——, ——, C. Deser, and B. Xiang, 2021: Zonal mean and shift modes of historical climate response to evolving aerosol distribution. *Sci. Bull.*, **66**, 2405–2411, https://doi.org/10.1016/j.scib.2021.07.013.

Kay, J. E., and Coauthors, 2015: The Community Earth System Model (CESM) large ensemble project: A community resource for studying climate change in the presence of internal climate variability. *Bull. Amer. Meteor. Soc.*, **96**, 1333–1349, https://doi.org/10.1175/BAMS-D-13-00255.1.

——, C. Wall, V. Yettella, B. Medeiros, C. Hannay, P. Caldwell, and C. Bitz, 2016: Global climate impacts of fixing the Southern Ocean shortwave radiation bias in the Community Earth System Model (CESM). *J. Climate*, **29**, 4617–4636, https://doi.org/10.1175/JCLI-D-15-0358.1.

Kuhlbrodt, T., A. Griesel, M. Montoya, A. Levermann, M. Hofmann, and S. Rahmstorf, 2007: On the driving processes of the Atlantic meridional overturning circulation. *Rev. Geophys.*, **45**, RG2001, https://doi.org/10.1029/2004RG000166.

Larson, S. M., and B. P. Kirtman, 2013: The Pacific meridional mode as a trigger for ENSO in a high-resolution coupled model. *Geophys. Res. Lett.*, **40**, 3189–3194, https://doi.org/10.1002/grl.50571.

——, and ——, 2014: The Pacific meridional mode as an ENSO precursor and predictor in the North American Multimodel Ensemble. *J. Climate*, **27**, 7018–7032, https://doi.org/10.1175/JCLI-D-14-00055.1.

——, D. J. Vimont, A. C. Clement, and B. P. Kirtman, 2018: How momentum coupling affects SST variance and large-scale Pacific climate variability in CESM. *J. Climate*, **31**, 2927–2944, https://doi.org/10.1175/JCLI-D-17-0645.1.

——, M. W. Buckley, and A. C. Clement, 2020: Extracting the buoyancy-driven Atlantic meridional overturning circulation. *J. Climate*, **33**, 4697–4714, https://doi.org/10.1175/JCLI-D-19-0590.1.

Lawrence, D. M., K. W. Oleson, M. G. Flanner, C. G. Fletcher, P. J. Lawrence, S. Levis, S. C. Swenson, and G. B. Bonan, 2012: The CCSM4 land simulation, 1850–2005: Assessment of surface climate and new capabilities. *J. Climate*, **25**, 2240–2260, https://doi.org/10.1175/JCLI-D-11-00103.1.

Lindzen, R. S., and A. V. Hou, 1988: Hadley circulations for zonally averaged heating centered off the equator. *J. Atmos. Sci.*, **45**, 2416–2427, https://doi.org/10.1175/1520-0469(1988)045<2416:HCFZAH>2.0.CO;2.

Liu, F., Y. Luo, J. Lu, and X. Wan, 2021: The role of ocean dynamics in the cross-equatorial energy transport under a thermal forcing in the Southern Ocean. *Adv. Atmos. Sci.*, **38**, 1737–1749, https://doi.org/10.1007/s00376-021-1099-6.

Liu, W., J. Lu, S.-P. Xie, and A. Fedorov, 2018: Southern Ocean heat uptake, redistribution, and storage in a warming climate: The role of meridional overturning circulation. *J. Climate*, **31**, 4727–4743, https://doi.org/10.1175/JCLI-D-17-0761.1.

Liu, Z., 1994: A simple model of the mass exchange between the subtropical and tropical ocean. *J. Phys. Oceanogr.*, **24**, 1153–1165, https://doi.org/10.1175/1520-0485(1994)024<1153:ASMOTM>2.0.CO;2.

——, 1999: Forced planetary wave response in a thermocline gyre. *J. Phys. Oceanogr.*, **29**, 1036–1055, https://doi.org/10.1175/1520-0485(1999)029<1036:FPWRIA>2.0.CO;2.

Lu, F., Z. Liu, Y. Liu, S. Zhang, and R. Jacob, 2017: Understanding the control of extratropical atmospheric variability on ENSO using a coupled data assimilation approach. *Climate Dyn.*, **48**, 3139–3160, https://doi.org/10.1007/s00382-016-3256-7.

Luyten, J., J. Pedlosky, and H. Stommel, 1983: The ventilated thermocline. *J. Phys. Oceanogr.*, **13**, 292–309, https://doi.org/10.1175/1520-0485(1983)013<0292:TVT>2.0.CO;2.

Ma, J., S.-P. Xie, and H. Xu, 2017: Contributions of the North Pacific meridional mode to ensemble spread of ENSO prediction. *J. Climate*, **30**, 9167–9181, https://doi.org/10.1175/JCLI-D-17-0182.1.

Manabe, S., and R. J. Stouffer, 1997: Coupled ocean–atmosphere model response to freshwater input: Comparison to Younger Dryas event. *Paleoceanography*, **12**, 321–336, https://doi.org/10.1029/96PA03932.

——, and ——, 1999: The role of thermohaline circulation in climate. *Tellus*, **51B**, 91–109, https://doi.org/10.3402/tellusb.v51i1.16262.

Marsh, R., 2000: Recent variability of the North Atlantic thermohaline circulation inferred from surface heat and freshwater fluxes. *J. Climate*, **13**, 3239–3260, https://doi.org/10.1175/1520-0442(2000)013<3239:RVOTNA>2.0.CO;2.

Marshall, J., A. Donohoe, D. Ferreira, and D. McGee, 2014: The ocean's role in setting the mean position of the Inter-Tropical Convergence Zone. *Climate Dyn.*, **42**, 1967–1979, https://doi.org/10.1007/s00382-013-1767-z.

McCreary, J. P., and P. Lu, 1994: Interaction between the subtropical and equatorial ocean circulations: The subtropical cell. *J. Phys. Oceanogr.*, **24**, 466–497, https://doi.org/10.1175/1520-0485(1994)024<0466:IBTSAE>2.0.CO;2.

Mitchell, T. P., and J. M. Wallace, 1992: The annual cycle in equatorial convection and sea surface temperature. *J. Climate*, **5**, 1140–1156, https://doi.org/10.1175/1520-0442(1992)005<1140:TACIEC>2.0.CO;2.

Neale, R. B., and Coauthors, 2010: Description of the NCAR Community Atmosphere Model (CAM5.0). NCAR Tech. Note NCAR/TN-486+STR, 268 pp., www.cesm.ucar.edu/models/cesm1.1/cam/docs/description/cam5_desc.pdf.

Newsom, E. R., and A. F. Thompson, 2018: Reassessing the role of the Indo-Pacific in the ocean's global overturning circulation. *Geophys. Res. Lett.*, **45**, 12 422–12 431, https://doi.org/10.1029/2018GL080350.

——, C. M. Bitz, F. O. Bryan, R. Abernathey, and P. R. Gent, 2016: Southern Ocean deep circulation and heat uptake in a high-resolution climate model. *J. Climate*, **29**, 2597–2619, https://doi.org/10.1175/JCLI-D-15-0513.1.

——, L. Zanna, S. Khatiwala, and J. M. Gregory, 2020: The influence of warming patterns on passive ocean heat uptake. *Geophys. Res. Lett.*, **47**, e2020GL088429, https://doi.org/10.1029/2020GL088429.

Nonaka, M., S.-P. Xie, and K. Takeuchi, 2000: Equatorward spreading of a passive tracer with application to North Pacific interdecadal temperature variations. *J. Oceanogr.*, **56**, 173–183, https://doi.org/10.1023/A:1011135113079.

Norris, J. R., and C. B. Leovy, 1994: Interannual variability in stratiform cloudiness and sea surface temperature. *J. Climate*, **7**, 1915–1925, https://doi.org/10.1175/1520-0442(1994)007<1915:IVISCA>2.0.CO;2.

——, Y. Zhang, and J. M. Wallace, 1998: Role of low clouds in summertime atmosphere–ocean interactions over the North Pacific. *J. Climate*, **11**, 2482–2490, https://doi.org/10.1175/1520-0442(1998)011<2482:ROLCIS>2.0.CO;2.

Oldenburg, D., R. C. Wills, K. C. Armour, L. Thompson, and L. C. Jackson, 2021: Mechanisms of low-frequency variability in North Atlantic Ocean heat transport and AMOC. *J. Climate*, **34**, 4733–4755, https://doi.org/10.1175/JCLI-D-20-0614.1.

Pausata, F. S., L. Chafik, R. Caballero, and D. S. Battisti, 2015: Impacts of high-latitude volcanic eruptions on ENSO and AMOC. *Proc. Natl. Acad. Sci. USA*, **112**, 13 784–13 788, https://doi.org/10.1073/pnas.1509153112.

——, C. Karamperidou, R. Caballero, and D. S. Battisti, 2016: ENSO response to high-latitude volcanic eruptions in the Northern Hemisphere: The role of the initial conditions. *Geophys. Res. Lett.*, **43**, 8694–8702, https://doi.org/10.1002/2016GL069575.

Pegion, K. V., and C. Selman, 2017: Extratropical precursors of the El Niño–Southern Oscillation. *Climate Extremes*, **226**, 301, https://doi.org/10.1002/9781119068020.ch18.

Philander, S., D. Gu, G. Lambert, T. Li, D. Halpern, N. Lau, and R. Pacanowski, 1996: Why the ITCZ is mostly north of the equator. *J. Climate*, **9**, 2958–2972, https://doi.org/10.1175/1520-0442(1996)009<2958:WTIIMN>2.0.CO;2.

Qiu, B., W. Miao, and P. Müller, 1997: Propagation and decay of forced and free baroclinic Rossby waves in off-equatorial oceans. *J. Phys. Oceanogr.*, **27**, 2405–2417, https://doi.org/10.1175/1520-0485(1997)027<2405:PADOFA>2.0.CO;2.

Schneider, T., 2017: Feedback of atmosphere–ocean coupling on shifts of the Intertropical Convergence Zone. *Geophys. Res. Lett.*, **44**, 11 644–11 653, https://doi.org/10.1002/2017GL075817.

——, T. Bischoff, and G. H. Haug, 2014: Migrations and dynamics of the intertropical convergence zone. *Nature*, **513**, 45–53, https://doi.org/10.1038/nature13636.

Sherwood, S., and Coauthors, 2020: An assessment of Earth's climate sensitivity using multiple lines of evidence. *Rev. Geophys.*, **58**, e2019RG000678, https://doi.org/10.1029/2019RG000678.

Shi, J.-R., L. D. Talley, S.-P. Xie, W. Liu, and S. T. Gille, 2020: Effects of buoyancy and wind forcing on Southern Ocean climate change. *J. Climate*, **33**, 10 003–10 020, https://doi.org/10.1175/JCLI-D-19-0877.1.

Shin, S.-I., and Z. Liu, 2000: Response of the equatorial thermocline to extratropical buoyancy forcing. *J. Phys. Oceanogr.*, **30**, 2883–2905, https://doi.org/10.1175/1520-0485(2001)031<2883:ROTETT>2.0.CO;2.

Smith, R., and Coauthors, 2010: The Parallel Ocean Program (POP) reference manual: Ocean component of the Community Climate System Model (CCSM) and Community Earth System Model (CESM). Rep. LAUR-10-01853, 141 pp., https://opensky.ucar.edu/islandora/object/manuscripts%3A825/datastream/PDF/view.

Speer, K., and E. Tziperman, 1992: Rates of water mass formation in the North Atlantic Ocean. *J. Phys. Oceanogr.*, **22**, 93–104, https://doi.org/10.1175/1520-0485(1992)022<0093:ROWMFI>2.0.CO;2.

Stevenson, S., B. Otto-Bliesner, J. Fasullo, and E. Brady, 2016: "El Niño like" hydroclimate responses to last millennium volcanic eruptions. *J. Climate*, **29**, 2907–2921, https://doi.org/10.1175/JCLI-D-15-0239.1.

Stommel, H., 1979: Determination of water mass properties of water pumped down from the Ekman layer to the geostrophic flow below. *Proc. Natl. Acad. Sci. USA*, **76**, 3051–3055, https://doi.org/10.1073/pnas.76.7.3051.

Sun, S., I. Eisenman, and A. L. Stewart, 2018: Does Southern Ocean surface forcing shape the global ocean overturning circulation? *Geophys. Res. Lett.*, **45**, 2413–2423, https://doi.org/10.1002/2017GL076437.

——, A. F. Thompson, and I. Eisenman, 2020: Transient overturning compensation between Atlantic and Indo-Pacific basins. *J. Phys. Oceanogr.*, **50**, 2151–2172, https://doi.org/10.1175/JPO-D-20-0060.1.

——, ——, S.-P. Xie, and S.-M. Long, 2022: Indo-Pacific warming induced by a weakening of the Atlantic meridional overturning circulation. *J. Climate*, **35**, 815–832, https://doi.org/10.1175/JCLI-D-21-0346.1.

Talley, L. D., G. L. Pickard, W. J. Emery, and J. H. Swift, 2011: *Descriptive Physical Oceanography: An Introduction*. 6th ed. Academic Press, 555 pp.

Thompson, L. A., and C. A. Ladd, 2004: The response of the North Pacific Ocean to decadal variability in atmospheric forcing: Wind versus buoyancy forcing. *J. Phys. Oceanogr.*, **34**, 1373–1386, https://doi.org/10.1175/1520-0485(2004)034<1373:TROTNP>2.0.CO;2.

Tomas, R. A., C. Deser, and L. Sun, 2016: The role of ocean heat transport in the global climate response to projected Arctic sea ice loss. *J. Climate*, **29**, 6841–6859, https://doi.org/10.1175/JCLI-D-15-0651.1.

Vimont, D. J., J. M. Wallace, and D. S. Battisti, 2003: The seasonal footprinting mechanism in the Pacific: Implications for ENSO. *J. Climate*, **16**, 2668–2675, https://doi.org/10.1175/1520-0442(2003)016<2668:TSFMIT>2.0.CO;2.

Walin, G., 1982: On the relation between sea-surface heat flow and thermal circulation in the ocean. *Tellus*, **34**, 187–195, https://doi.org/10.3402/tellusa.v34i2.10801.

Waliser, D. E., and C. Gautier, 1993: A satellite-derived climatology of the ITCZ. *J. Climate*, **6**, 2162–2174, https://doi.org/10.1175/1520-0442(1993)006<2162:ASDCOT>2.0.CO;2.

Wang, G., S.-P. Xie, R. X. Huang, and C. Chen, 2015: Robust warming pattern of global subtropical oceans and its mechanism. *J. Climate*, **28**, 8574–8584, https://doi.org/10.1175/JCLI-D-14-00809.1.

Wang, H., S.-P. Xie, and Q. Liu, 2016: Comparison of climate response to anthropogenic aerosol versus greenhouse gas forcing: Distinct patterns. *J. Climate*, **29**, 5175–5188, https://doi.org/10.1175/JCLI-D-16-0106.1.

Wood, R., 2012: Stratocumulus clouds. *Mon. Wea. Rev.*, **140**, 2373–2423, https://doi.org/10.1175/MWR-D-11-00121.1.

Wunsch, C., 2005: The total meridional heat flux and its oceanic and atmospheric partition. *J. Climate*, **18**, 4374–4380, https://doi.org/10.1175/JCLI3539.1.

Xie, S.-P., 2004: The shape of continents, air–sea interaction, and the rising branch of the Hadley circulation. *The Hadley Circulation: Present, Past and Future*.H. F. Diaz and R. S. Bradley, Eds., Springer, 121–152.

——, and S. G. H. Philander, 1994: A coupled ocean–atmosphere model of relevance to the ITCZ in the eastern Pacific. *Tellus*, **46A**, 340–350, https://doi.org/10.3402/tellusa.v46i4.15484.

——, C. Deser, G. A. Vecchi, J. Ma, H. Teng, and A. T. Wittenberg, 2010: Global warming pattern formation: Sea surface temperature

and rainfall. *J. Climate*, **23**, 966–986, https://doi.org/10.1175/2009JCLI3329.1.

Yang, L., S.-P. Xie, S. S. P. Shen, J.-W. Liu, and Y.-T. Hwang, 2022: Low cloud–SST feedback over the subtropical northeast Pacific and the effect on ENSO variability. *J. Climate*, submitted.

Yu, S., and M. S. Pritchard, 2019: A strong role for the AMOC in partitioning global energy transport and shifting ITCZ position in response to latitudinally discrete solar forcing in CESM1. 2. *J. Climate*, **32**, 2207–2226, https://doi.org/10.1175/JCLI-D-18-0360.1.

Zhu, J., Z. Liu, X. Zhang, I. Eisenman, and W. Liu, 2014: Linear weakening of the AMOC in response to receding glacial ice sheets in CCSM3. *Geophys. Res. Lett.*, **41**, 6252–6258, https://doi.org/10.1002/2014GL060891.